

Late Quaternary Surface Displacements on Accretionary Wedge Splay Faults in the Cascadia Subduction Zone: Implications for Megathrust Rupture

A.M. Ledeczi *¹, M.C. Lucas ¹, H.J. Tobin ¹, J.T. Watt ², N.C. Miller ³

¹Department of Earth & Space Sciences, University of Washington, Seattle, WA, ²U.S. Geological Survey, Pacific Coastal and Marine Science Center, Santa Cruz, CA, ³U.S. Geological Survey, Woods Hole Coastal and Marine Science Center, Woods Hole, MA

Author contributions: *Conceptualization:* A.M. Ledeczi., H.J. Tobin, J.T. Watt. *Methodology:* A.M. Ledeczi. *Investigation:* A.M. Ledeczi, M.C. Lucas. *Supervision:* H.J. Tobin, J.T. Watt. *Resources:* J.T. Watt, N.C. Miller. *Funding acquisition:* H.J. Tobin. *Writing - original draft:* A.M. Ledeczi. *Writing - review & editing:* A.M. Ledeczi, M.C. Lucas, H.J. Tobin, J.T. Watt, N.C. Miller.

Abstract Because splay faults branch at a steep dip angle from the plate-boundary décollement in an accretionary wedge, their coseismic displacement can potentially result in larger tsunamis with distinct characteristics compared to megathrust-only fault ruptures, posing an enhanced hazard to coastal communities. Elsewhere, there is evidence of coseismic slip on splay faults during many of the largest subduction zone earthquakes, but our understanding of potentially active splay faults and their hazards at the Cascadia subduction zone remains limited. To identify the most recently active splay faults at Cascadia, we conduct stratigraphic and structural interpretations of near-surface deformation in the outer accretionary wedge for the ~400 km along-strike length of the landward vergence zone. We analyze recently acquired high-frequency sparker seismic data and crustal-scale multi-channel seismic data to examine the record of deformation in shallow slope basins and the upper ~1 km of the surrounding accreted sediments and to investigate linkages to deeper décollement structure. We present a new fault map for widest, most completely locked portion of Cascadia from 45 to 48° N latitude, which documents the distribution of faults that show clear evidence of recent late Quaternary activity. We find widespread evidence for active splay faulting up to 30 km landward of the deformation front, in what we define as the active domain, and diminished fault activity landward outside of this zone. The abundance of surface-deforming splay faults in the active outer wedge domain suggests Cascadia megathrust events may commonly host distributed shallow rupture on multiple splay faults located within 30 km of the deformation front.

Non-technical summary Earthquakes and their resulting tsunamis at the Cascadia subduction zone, where the Juan de Fuca plate subducts under the North American plate from northern California to Vancouver Island, pose great hazard to coastal communities. As sediment from the subducting plate is scraped off, piles of sediment known as accretionary wedges can form at these plate boundaries. During large earthquakes, the rupture of the main plate boundary fault may be accompanied by slip on multiple branching faults within the accretionary wedge, which would potentially impact the size and characteristics of tsunami produced by the event. The likelihood of splay fault slip remains largely unknown at Cascadia because the last large earthquake occurred in 1700. We interpret newly collected subsurface images using seismic wave reflections to identify the most recently active offshore faults. We document evidence of widespread recent fault activity within the accretionary wedge in a roughly ~30 km wide zone stretching from Washington to northern Oregon. By mapping these active branching faults, we seek to provide inputs to tsunami and earthquake models which may in turn refine predictions and preparations for coastal impacts during future earthquakes at Cascadia.

1 Introduction

Accretionary wedges at subduction zones are fold and thrust belts formed when sediment is scraped off the downgoing plate and accumulates at the leading edge of the overriding plate. The plate boundary décollement forms the base of the accretionary wedge, and numerous higher-angle splay faults, including the frontal thrust, branch from it, bounding the individual thrust sheets that comprise the wedge. As new material is ac-

creted, splay faults activate to accommodate this deformation, adjusting the surface slope of the accretionary wedge through fault activity or erosion to reach a critical taper angle of stability (Davis et al., 1983). It was once thought that accretionary wedges cannot nucleate nor host seismogenic slip near the trench on either the plate boundary décollement or on splay faults because those faults were seen as being hosted in weak, unlithified materials (i.e., frictionally stable) (e.g., Byrne et al., 1988), but this view was gradually supplanted by an understanding that temperature-dependent fric-

Production Editor:
Christie Rowe
Handling Editor:
Emilie Hooft
Copy & Layout Editor:
Hannah F. Mark

Signed reviewer(s):
Lisa McNeill
Utsav Mannu

Received:
January 12, 2024
Accepted:
April 17, 2024
Published:
April 30, 2024

*Corresponding author: ledeczi@uw.edu

tional properties, rather than the absence of sedimentary material, governs seismic locking and slip. A 100–150°C isotherm threshold, which corresponds to many transitions in material properties of the host sediments or rock, is now more commonly identified as the updip limit for frictional locking and slip at subduction zones (Hyndman and Wang, 1993; Moore and Saffer, 2001).

Recent earthquakes have shown that both shallow slip and splay fault activation are possible and even prevalent during large megathrust events. For example, in the M_w 9.1 2011 Tohoku-Oki earthquake, the majority of the rupture occurred above 40 km in depth, and slip peaked at the trench (Ide et al., 2011; Sun et al., 2017). Differential bathymetry, displaced seafloor geodetic monuments, and scarp mapping all indicate that 50 to 120 meters of coseismic slip occurred at the trench axis during this event (Fujiwara et al., 2011; Ito et al., 2011; Kodaira et al., 2012, 2020; Ueda et al., 2023). Similarly, the 2004 M_w 9.1 Sumatra earthquake had largely shallow coseismic rupture beneath the accretionary wedge that may have extended to the deformation front based on scarps mapped there (Gulick et al., 2011; Henstock et al., 2006; Ishii et al., 2005). Bathymetric surveys following the event document widespread faulting, folding, and mass wasting of the accretionary wedge, attributed to coseismic splay fault rupture (Seber et al., 2007). Subaerial surface uplift and bathymetric investigation following the 1964 M_w 9.2 Alaska earthquake found coseismic slip of up to 12 m on two splay faults in the wedge (Liberty et al., 2013; Plafker, 1969). Core samples from the offshore frontal thrust and megasplay fault of the Nankai Trough wedge record frictional heating of sediments which indicate that coseismic slip likely propagated to the toe of the accretionary wedge and along the megasplay fault in the past (Sakaguchi et al., 2011; Yamaguchi et al., 2011).

Tsunamis generated by large megathrust events are typically much more destructive than shaking from earthquakes themselves, and shallow slip concentrated in the outer accretionary wedge may play a great role in tsunami generation (Wilson and Ma, 2021). Shallow slip along the megathrust can cause large seafloor uplift in deep water and is thus more efficient at tsunami generation than slip which stops farther downdip. However, because of their relatively steeper dip angle compared to the frontal décollement, splay fault activation can result in even larger tsunamis with multiple flooding episodes compared to megathrust-only fault ruptures, posing a unique hazard to coastal communities (Gao et al., 2018; Wendt et al., 2009; van Zelst et al., 2022).

At Cascadia, dislocation modeling has confirmed that shallow splay fault slip can cause a larger tsunami, as compared to slip only on the megathrust (Gao et al., 2018). The area offshore Washington state has atypical accretionary wedge morphology and is coincident with the zone of greatest geodetic locking at Cascadia (Li et al., 2018; Lindsey et al., 2021; Schmalzle et al., 2014), which suggests this region may experience the most slip during a future megathrust event. However, since the last megathrust event at Cascadia occurred in 1700 (Satake et al., 1996), and there is a notable absence of re-

cent seismicity in the region (e.g., Stone et al., 2018), our knowledge of what future slip scenarios could look like or what faults could experience slip is limited.

In this study, we systematically evaluate which splay faults offshore Washington and Oregon show evidence of hosting recent near-surface displacement and map their continuity along strike for a > 400 km span from 45° to 48°N latitude. We use high-frequency sparker multi-channel seismic reflection data to characterize sedimentary sequences and structural history of slope basins and the upper 1 km of the accreted wedge, which allows us to identify faults that have been recently active in late Quaternary time throughout the outer wedge in the landward vergence zone (LVZ), the area of Cascadia which displays atypical morphology (Fig. 1) and coincides with the largest patch of the megathrust that is apparently fully locked (Lindsey et al., 2021). We analyze slope basins, which are sensitive recorders of activity on accretionary wedge faults as the basins fill with sediments over time from their formation to the present. In particular, we seek to determine whether splay faults are active only at the frontal thrust, at the inner-outer wedge transition, or throughout the outer wedge. We hypothesize that rather than progressing in sequence toward the deformation front, thrusts in the accretionary wedge at Cascadia display a more complex history of thrust activation. Our findings support the hypothesis that many splay faults are potential candidates for hosting coseismic slip, and that Cascadia will likely experience distributed shallow rupture on multiple splay faults located within ~30 km of the deformation front in a future megathrust event.

2 Tectonic Setting and Accretionary Wedge Mechanics

Offshore Washington, the Juan de Fuca plate is subducting northwestward under the North American plate at ~39 mm/yr (Fig. 1; DeMets et al., 2010). A 2 to 3 kilometer thick sequence of clastic sediment overlies the oceanic basement of the incoming plate. Most of this sediment is scraped off as the oceanic plate subducts, forming a wide and rapidly growing accretionary wedge throughout our study area. As splay faults propagate within the wedge, they fold the sedimentary strata of the wedge into anticlinal structures to form trench-parallel ridges. Between the ridges, shallow (~100s of meters deep) wedge-top basins known as piggyback or slope basins are created and fill with continuously depositing sediments. The entire outer wedge in this region, including thrust sheets and slope basin sediments, has been formed over less than 2 million years during the Pleistocene and Holocene (Barnard, 1978).

The accretionary wedge is comprised of several distinct morphotectonic regions with variable characteristics along strike (Watt and Brothers, 2020). From 45° to 48°N latitude, the LVZ contains almost exclusively landward-vergent (seaward-dipping) splay faults (MacKay, 1995; Seely, 1977), while thrusting in the wedge elsewhere is mostly seaward-vergent, which is more typical in subduction zones worldwide (Fig. 1).

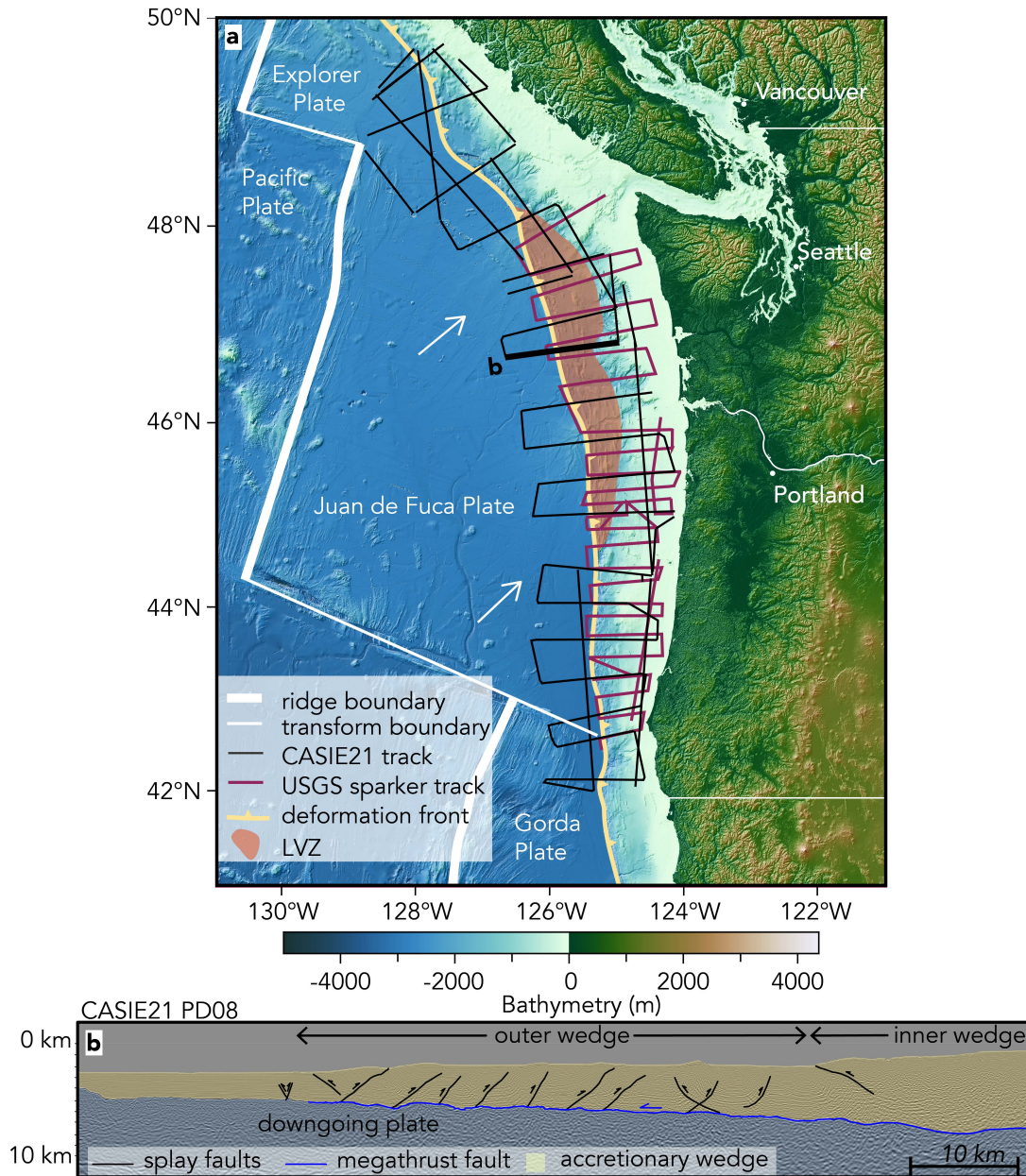


Figure 1 a. Map of the Cascadia subduction zone with deformation front in yellow. The region where landward-vergent thrusting dominates (LVZ) is shaded pink. Black and pink tracklines are for low-frequency CASIE21 MCS reflection data collected on the *R/V Marcus G. Langseth* and for the high-frequency sparker and chirp taken in 2019 on the *R/V Rachel Carson*, respectively. Incoming plate boundaries shown in white. Relative plate motion between the Juan de Fuca plate and the North American plate indicated by white arrows at rates varying between 42 mm/yr in the north and 34 mm/yr in the south (DeMets et al., 2010). b. CASIE21 Line PD08 showing the megathrust fault, splay faults, and the location of the inner and outer accretionary wedge.

Seismic reflection data show that, in the LVZ, landward-vergent thrusts have kilometers of displacement each whereas seaward-vergent thrusts are nearly nonexistent (Adam et al., 2004). Many explanations have been proposed for the LVZ, such as an internally strong wedge with a weak base, perhaps due to high pore pressure (MacKay, 1995; Tobin et al., 1993); a high sedimentation rate (Adam et al., 2004); and/or a compositional difference in wedge sediments (Gutscher et al., 2001; Underwood, 2002). The widespread nature of the landward vergence at Cascadia is unusual among fold-and-thrust belts worldwide, with only two comparable examples.

The northern Sumatra region of the Sunda subduction zone also displays dominantly landward vergence at the toe of the accretionary wedge, with seaward-vergent faults located farther landward (Frederik et al., 2015; McNeill and Henstock, 2014). Isolated areas of landward vergence have been observed at the Niger Delta, a submarine fold and thrust belt driven by gravitational collapse rather than tectonics (Bilotti and Shaw, 2005; Maloney et al., 2010).

The oblique component of the subduction angle is thought to be accommodated by numerous left-lateral strike-slip faults striking northwest-southeast across

the margin. These structures were first identified in the 1990s by sidescan sonar, seismic reflection, and bathymetric data, and were found to have Holocene activity by observing offset geomorphic markers (Goldfinger et al., 1992, 1997, 1996). Some of these faults are thought to offset the downgoing plate (Han et al., 2018) whereas some may originate in and be confined to the accretionary wedge sediments of the upper plate. These faults can accommodate arc-parallel strain, facilitating bookshelf faulting of the forearc (Goldfinger et al., 1996). A zone of listric normal faulting on the continental shelf offshore Grays Harbor suggests this region is undergoing extension and is unaffected by the compressive forces dominating the outer wedge (McNeill et al., 1997).

The strength contrast at the inner-outer wedge transition or the dynamic backstop boundary (Frederik et al., 2015; Kopp and Kukowski, 2003; Wang and Hu, 2006) has been hypothesized to localize splay fault activity at other subduction zones, such as Nankai (Gulick et al., 2010; Moore et al., 2007; Tobin et al., 2019) and Alaska (Liberty et al., 2013; Ramos et al., 2022; von Huene et al., 2021). We prefer the term inner-outer wedge transition over dynamic backstop boundary and use it throughout this paper. At Cascadia, the inner-outer wedge transition marks the boundary between the less consolidated, Pleistocene-dominated outer accretionary wedge and the more consolidated, Miocene inner accretionary wedge sediments (Frederik et al., 2015; Kopp and Kukowski, 2003; Tobin et al., 2019; Wang and Hu, 2006). At Nankai, the continuity of a major active fault along strike at the boundary led to the use of the term “megaspaly” to distinguish this major domain-bounding fault system from other splays in the outer wedge (Tobin and Kinoshita, 2006). In both Nankai and Alaska, there is evidence that splay faults have localized slip in past megathrust events and serve as a potential tsunami source (Moore et al., 2007; Ramos et al., 2022; von Huene et al., 2021). Similar megaspaly faults at the inner-outer wedge transition have been proposed and used for tsunami modeling at Cascadia (e.g., Gao et al., 2018; Witter et al., 2013).

3 Methods

3.1 Data Acquisition and Processing

The 11 lines of high-resolution multichannel seismic reflection data used in this study were collected aboard the *R/V Rachel Carson* in 2019 (Balster-Gee et al., 2023). The seismic sound source was an Applied Acoustics Delta sparker operated at 1.4 to 3.6 kJ and towed at a nominal depth of 0.75 m. The data were recorded using a 72-channel, ~450-m-long Geometrics GeoEel hydrophone streamer sampled at 0.25 ms. Streamer tow depth ranged from ~1 to 9 m, depending on sea state. Two calibrated hydrophones were towed below the sparker source to record near-field source signatures at each source point, enabling deconvolution of the mixed-phase and highly variable source (Kluesner et al., 2018). All positioning was determined relative to the ship’s GPS, with streamer and source positions as-

sumed to follow the ship track.

The sparker data were processed through a workflow including: crooked-line common-midpoint (CMP) binning at 3.125 m spacing; resampling from 0.25 to 0.5 ms, 70–400 Hz band-pass filtering; source designation and deghosting using recorded source signatures; trace editing; despiking; F-K filtering; semblance analysis for stacking velocities; normal-moveout correction; receiver static correction and three-trace median filtering in the channel domain; stacking; and post-stack time migration. Versions of the migrated images with a 200 ms automatic gain control (AGC) and spiking deconvolution applied were used for interpretation. The sparker source provides usable reflections up to 1 km below the seafloor but penetration depends heavily on the subsurface geology. Horizontal resolution of the data is set by the 3.125 m CMP spacing. Vertical resolution based on the peak frequencies in the migrated images is between 0.42 and 3.75 m.

We conduct joint interpretation of sparker data with lower-resolution but deeper-penetrating 2-D multichannel seismic reflection data from the Cascadia Seismic Imaging Experiment (CASIE21) collected on the *R/V Marcus G. Langseth* in 2021 (Carbotte et al., 2023). The data were collected using a 12 to 15 km streamer with a 6600 cu in 36-airgun array source. Processing of the data to pre-stack depth migration was carried out by ION Geophysical. This study is based upon the analysis of the 11 northernmost sparker dip lines and 8 nearby CASIE21 lines which cover the LVZ (Fig. 1a). These lines are spaced from 30 km to a maximum of 60 km apart. The lines traverse the accretionary wedge from the incoming plate to the upper continental shelf, with lengths ranging from 100 to 125 km. The usable sparker penetration reaches about 1 second two-way travel time (TWTT) below seafloor, or slightly less than 1 km, while the CASIE21 lines image to >10 km below seafloor. All seismic reflection profiles shown here face north, with seaward (W) to the left and landward (E) to the right. To aid in the identification of active faulting, we used published GMRT 50-m gridded bathymetry (Ryan et al., 2009) to conduct geomorphic analysis of bathymetric features such as scarps and anticlines.

3.2 Seismic and Bathymetric Interpretation

The time-domain sparker seismic sections were used to conduct a detailed stratigraphic and structural analysis of near-surface deformation in the wedge and in shallow lower slope basins that lie atop the accreted material. Principles of seismic stratigraphy were employed to identify packages within each basin displaying similar seismic reflection characteristics, known as seismic facies (Mitchum et al., 1977; Posamentier et al., 2022). Significant reflectors separating these packages were picked as horizons using the HIS Kingdom Suite seismic interpretation software package. We focus on slope basins because they represent the modern depocenters, where sediments are more likely to accumulate continually than on steeper anticlinal structures, allowing characterization of late-Pleistocene to Holocene deformation.

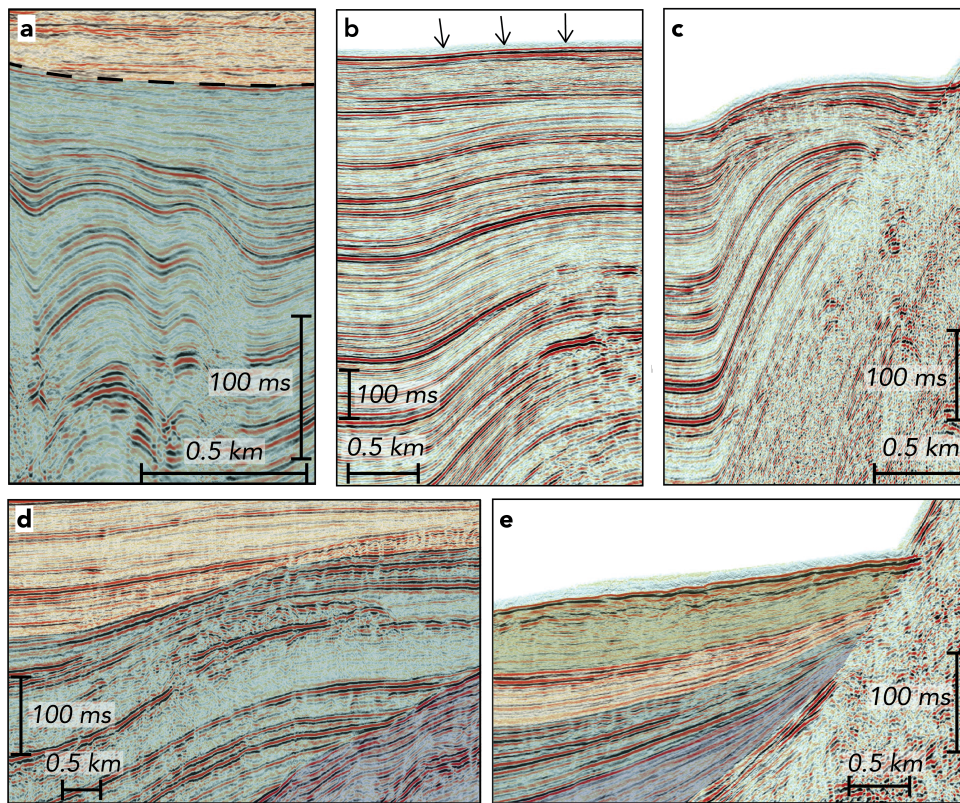


Figure 2 Examples of typical deformational and sedimentary characteristics observed in time sections of sparker seismic data in this study. **a.** A currently inactive fold with pre- or syndeformational strata shaded in blue below postdeformational, flat strata in orange. **b.** An active fault-propagation fold which shows offset at the surface highlighted with arrows. **c.** An active fold with a large seafloor signature. **d.** Seismic facies are defined in part by reflector geometries, e.g., where onlap occurs at seismic facies boundaries. Each color in this image represents a distinct seismic facies. **e.** Colored packages thin and onlap onto the anticline on the right boundary of the basin. The topmost green package shows thinning and surface tilting, indicating recent activity of the anticline.

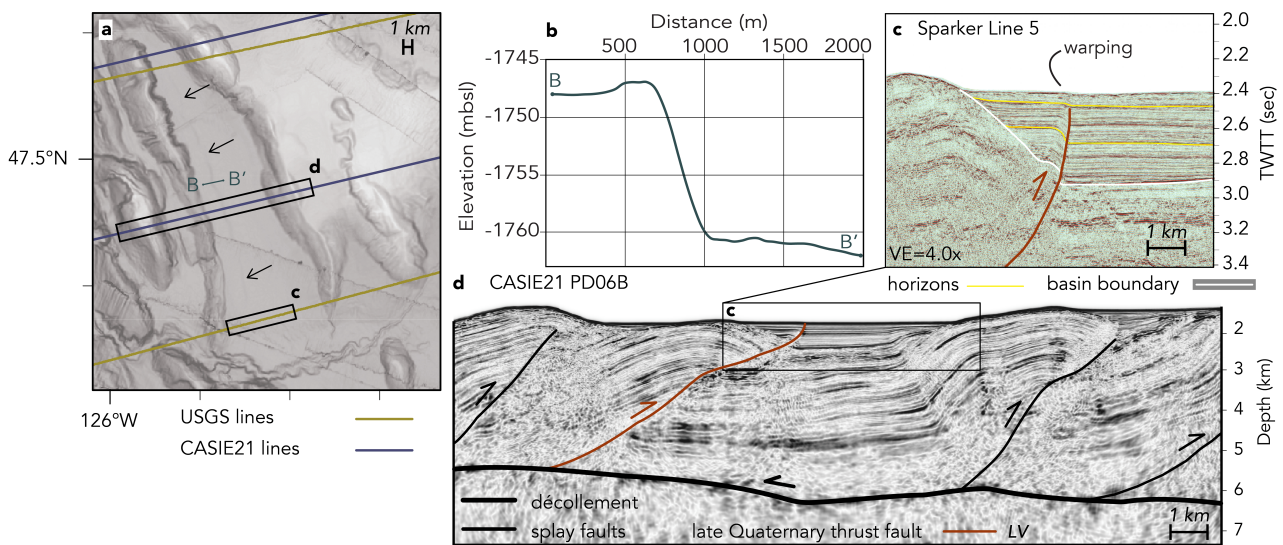


Figure 3 Tracing a late Quaternary active thrust to the surface. **a.** Arrows point to fault signature on multibeam bathymetry. **b.** Profile on bathymetry across the fault from B to B' showing a 13 m seafloor fold signature. **c.** Sparker line showing basal fault that warps uppermost sediment package, indicating late Quaternary activity. VE=4.0x within the sediments using a velocity of 1700 m/s. **d.** Same splay fault identified within CASIE21 Line PD06B as connecting to the décollement.

Faults we map here are either surface-breaking or buried (“blind”). For surface-breaking faults, we determine if they are active by whether they deform the surface with a discrete fault scarp, which definitively indicates Holocene activity (e.g., [McCalpin and Nelson, 2009](#)). Activity on buried faults is assessed by documenting the geometry of strata deposited in overlying or adjacent basins. Some active faults have seafloor fold scarps but we do not discriminate between small and large active folds because it is unknown how much of this difference can be explained by potentially varying sedimentation rates between basins or by differences in rate or timing of folding (e.g., Fig. 2b-c).

Types of deformation and stratigraphic characteristics considered in our analysis are shown in Fig. 2. The most common reflection terminations in our seismic data are onlap, a base-discordant relationship where horizontal or inclined strata terminate against a surface with greater inclination ([Mitchum et al., 1977](#)). This is commonly seen at basin boundaries (Fig. 2e) or at seismic sequence boundaries within basin sediments (Fig. 2d). We also note intrabasinal unconformities similar to others which have been noted in the past (e.g., [McNeill et al., 2000](#)). Thickening or thinning of stratal units onto an anticline or a fault, known as growth strata, are deposited during deformation, and are used as a proxy for discerning activity on buried faults underlying anticlines next to each basin ([Suppe et al., 1992](#)). Previous work has shown that sediment deposition occurs largely on slopes below 5°, and that sediment bypass is most likely on steeper slopes (e.g., [Hill et al., 2017](#); [Ross et al., 1994](#)). Therefore, we consider tilting of basinal units above 5° a result of tectonic activity rather than sediment deposition (Fig. 2e) and we mark this angle on each sparker profile accounting for vertical exaggeration. We measure the average angle of each basinal unit adjacent to the flanking anticlines using an assumed 1700 m/s sediment velocity to determine if it exceeds this threshold. In areas where the seafloor is steeper than 5° and nearby basins are not able to record growth, this method cannot be applied.

It is well-established that the age of the outer accretionary wedge in this region is Pleistocene (e.g., [Silver, 1972](#))—with fossil evidence indicating that the outermost ridges are less than 2 Ma ([Barnard, 1978](#))—and that there is a major structural boundary and age difference between the outer wedge and inner wedge domains (e.g., [Fisher et al., 1999](#); [Flueh et al., 1998](#); [McNeill et al., 1997](#)). We determine the recency of deformation based on relative ages of stratigraphic units in slope basins atop the wedge; since basinal sediment deposition continues to the present-day, the characteristics of the uppermost sediments allow us to determine the recency of deformation, which is likely much younger than the age of the wedge itself. Sediment accumulation rates within outer wedge slope basins offshore Washington varied between 2 and 40 cm/10³ years during the late postglacial 0-6750 B.P. and 6 and 29 cm/10³ years during the early postglacial 6750-10,000 B.P. ([Barnard, 1978](#); [Caulet, 1995](#)). Assuming a sediment seismic velocity of 1600 m/s and using the maximum sediment accumulation rate, the Holocene represents 0.006 seconds TWTT,

which is at most the top few reflectors of the sparker data used in this study. This vertical resolution constraint prevents us from determining whether observed deformation is explicitly Holocene unless discrete fault offset reaches the seafloor, producing a seafloor scarp. Instead, we categorize active faults as late Quaternary, which encompasses the Holocene and the latest Pleistocene, corresponding conservatively to the last 100,000 years, but in many cases much less. Older faults are classified as broadly older Quaternary, indicating activity before 100,000 years ago but since the known outer wedge formation at 2.58 Ma. Our use of high-resolution data allows us to discriminate the faults that exhibit evidence of activity in the very late Quaternary, and in some cases Holocene, from those which do not show evidence of true surface deformation, which we consider inactive. Essentially all of the inactive faults identified herein are listed as active in published datasets like the Quaternary Faults Database ([Schmitt, 2017](#)) and the DOGAMI neotectonic map ([Goldfinger et al., 2023](#)); hence our work constitutes a significant advance in identifying the most recently active structures.

We employ the GMRT 50m gridded bathymetry ([Ryan et al., 2009](#)) to map bathymetric signatures (fault-propagation folds or fault scarps) of active faults along strike between seismic lines (Fig. 3a). We quantify fault strike and length for all located faults as well as the height of seafloor signatures identifiable on the bathymetry (Fig. 3b). The bathymetry is also used to confirm the vergence of each fault by noting the steeper side of each anticline. For fault-propagation fold anticlines where the fault itself is not imaged in the sparker data, but is visible in the CASE21 MCS data, we map their location at the place where the anticline meets the seafloor, accounting for the fault vergence. These anticlines can be determined to be actively deforming or not based on the onlapping relationship of basin-fill strata. Inferred strike-slip faults are mapped based on the offset of anticlines visible in the bathymetry.

Once faults are identified in individual high-resolution seismic sections in this manner, we compare them to imaged faults in nearby or coincident lower-resolution CASIE21 seismic lines to ensure that identified splay faults are linked to the megathrust at depth (Fig. 3d). This analysis helps determine the vergence for faults that are near-vertical as they approach the surface or for those underlying fault-propagation fold anticlines. Combining these observations from the sparker data, CASIE21 data, and the bathymetry allows us to recognize faults which are continuous across multiple lines and link these in our maps. Minor faults which have little offset, are not spatially extensive, and/or are not imaged at depth in the CASIE21 data are shown in seismic profiles but are not included in our final maps.

4 Results

4.1 Defining the active and inactive domains

We located faults throughout the outer wedge of the LVZ using seismic reflection data (Fig. 4). A comparison of

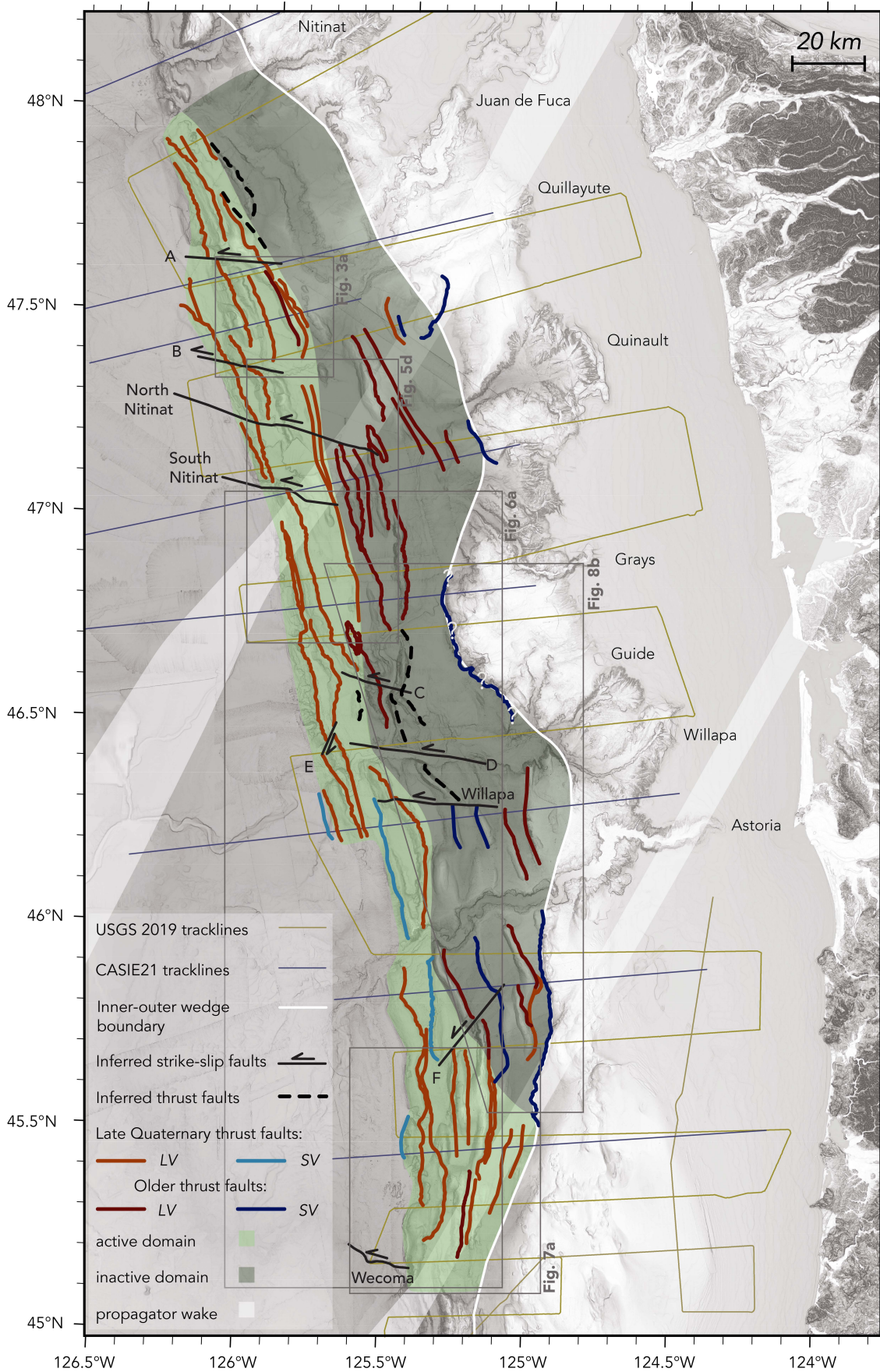


Figure 4 Structural map of the outer accretionary wedge in the landward vergence zone. Landward-vergent thrusts are in red and seaward-vergent thrusts in blue, with lighter shade for late Quaternary active thrusts as identified in this study. Inferred strike-slip faults are black lines and inferred thrusts are dashed black. The inner-outer wedge transition is white. Canyons are labeled. The locations of subset maps used in subsequent figures are shown in light grey. Propagator wake shear zones on the downgoing plate shown in white from (Nedimović et al., 2009).

slope basins within 30 km of the deformation front to those located in the innermost outer wedge closer to the inner-outer wedge boundary shows that they record a profound difference in deformational history and tectonic stratigraphy. This leads us to establish two main zones of the outer wedge, the *active domain* and the *inactive domain*. The boundary between the active and inactive domain follows a similar map pattern to the inner-outer wedge transition along the margin. We display transects across the active-inactive domain boundary to show how basinal characteristics differ on either side (Fig. 5).

The active domain of the outer wedge varies in width from ~15 to 30 km, defined by the prevalence of late Quaternary faulting at the deformation front and landward. It is characterized by prominent seafloor fault signatures and seismically imaged faulting or basinal growth strata to the seafloor. Most basins in the active domain are filled with syndeformational packages which indicates continuous fault activity during sediment deposition throughout the lifetime of the basin (Fig. 5a, f). Some basins within the active domain contain prominent faults which offset the seafloor (Fig. 5a, f). Others do not contain identified surface-breaking faults but show tilting of topmost packages at greater than 5° indicating activity of faults underlying adjacent anticlines.

We define the inactive domain as the landward portion of the outer wedge which lies between the active domain and the inner wedge and contains mostly older Quaternary faults. It varies in width from ~20 to 40 km and is characterized by flat, wide, and thickly sedimented basins with deeply buried faults. Only one seafloor fault signature is evident in the multibeam bathymetry in this region. These basins record syndeformational deposition of sediments in their bottom-most units with widespread imaged faults (Fig. 5b), thinning of units, or small-scale folding (Fig. 5g). However, in contrast to the active domain, basins in the inactive domain have postdeformational topmost packages which show no stratal thinning or thickening (Fig. 5b, g). Usually, a distinct unconformity separates these two types of tectonic strata (e.g., Fig. 5g).

4.2 The active domain

Concentrated late Quaternary faulting defines the active domain, where 35 of 38 active faults in the map area are located (Fig. 4). Landward-vergent thrust faults dominate the active domain, with only four seaward-vergent active faults imaged. Fault strike of thrusts in the active domain varies between 322° at the north end to 17° at the south end of the map area, following a change in the obliquity of subduction along the margin. Fault length varies from 7.5 to 70.2 km, with an average length of 29.7 km.

The active domain includes the deformation front which rather than being a single continuous fault is segmented along strike by mostly WNW-striking strike-slip faults into at least seven parts (Fig. 4). The deformation front region is characterized by thin basinal sediments with some faults which produce measur-

able seafloor scarps, indicating Holocene activity. The frontal thrust in the map area is primarily landward-vergent, but some short seaward-vergent frontal thrusts are present south of Willapa Canyon. Incipient thrust formation in multiple locations indicates the continued advance of the deformation front seaward. Eastward of the deformation front, the geomorphology of the active domain is typical of that of the LVZ, with widely spaced thrust sheets overlain by thick basinal sediments. Instead of seafloor scarps that characterize frontal thrust, evidence of faulting such as folding or warping of topmost sediment packages are more prevalent in the bathymetry.

At the northern end of the LVZ, the active domain is narrow, about 15 km in width, and contains landward-vergent faults which underlie closely spaced anticlines separated by small basins. The frontal thrust is cut by strike-slip Fault A at a large landslide scarp on the frontal anticline around 47.6°N, causing a 2 km left-lateral offset of the frontal thrust (Fig. 4). Here, the active domain widens to 28 km but the fault spacing remains similar to north of Fault A at 8 km or less between each landward-vergent splay fault. A new landward-vergent thrust is the dominant frontal thrust south of Fault A, which is again cut by strike-slip Fault B, showing less (~1 km) apparent left-lateral offset. The first fault east of the deformation front is an active landward-vergent thrust with a prominent 13 m high seafloor scarp 24 km in length, located in the middle of an 8 km wide basin (Fig. 3). This fault is well-imaged in two sparker lines as well as a CASIE21 MCS line, allowing us to trace it from the décollement to the near-surface (Fig. 3c-d). Though the fault tip does not break the surface at the available resolution of imaging, the uppermost sediment package is warped, and there are abundant growth strata in the basin, indicating late Quaternary activity of this fault (Fig. 3c).

Two active landward-vergent faults appear south of Fault B in an 18 km wide basin that crosses the active-inactive domain boundary (Fig. 3d). The westward fault in the fault pair has a seafloor fold 48 m high (Fig. 5a). These faults branch in the near-surface but connect at depth as well as merging into one fault along strike at the South Nitinat Fault (Fig. 5d). Between the North and South Nitinat strike-slip faults, a new 16 km long incipient frontal thrust forms seaward of the previously dominant frontal thrust. In this area, the deformation front is composed of two imbricated fault-propagation folds underlain by landward-vergent faults approximately 1 km apart.

Just south of the South Nitinat Fault, the two frontal thrusts are spread farther apart to 4 km, and the westward thrust is the dominant frontal thrust for 61 km along the margin, while the second thrust is continuous for 52 km (Fig. 6a). In this region, the active domain is 20 km wide and is characterized by fewer anticlines separated by wider basins with a thicker and smoother sediment cover. The deformation front is defined by an imbricated fault-propagation fold where two landward-vergent faults break to the seafloor; the eastward one has a scarp of 70 m visible on bathymetry (Fig. 6b). At 46.7°N, the frontal thrust scarp is 44 m in height where it

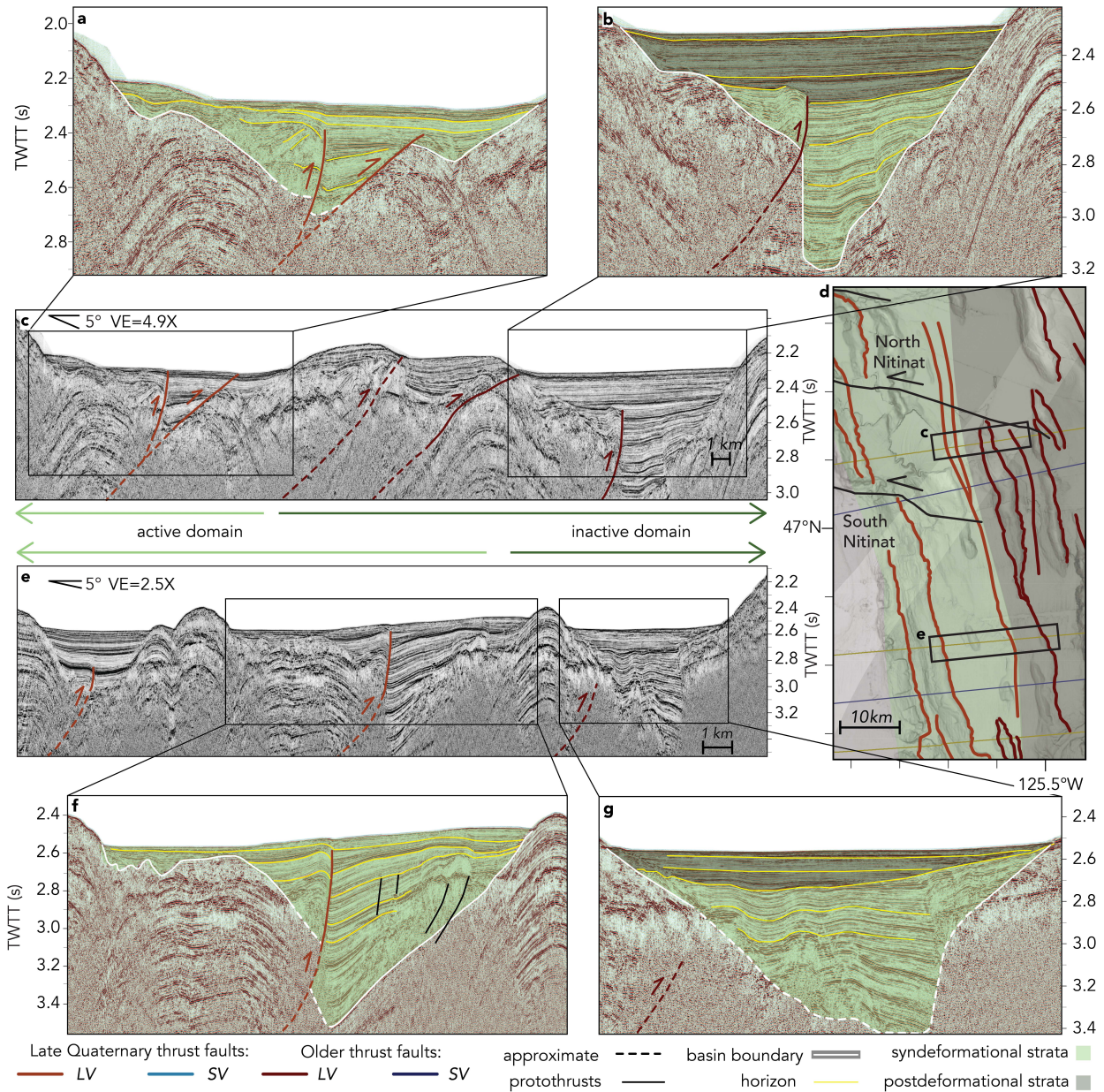


Figure 5 Comparison of tectonic stratigraphy across the active-inactive domain boundary. **a.** Detail of active domain basin from panel (c). Two active landward-vergent faults with syndeformational strata. **b.** Detail of inactive domain basin from panel (c). Buried landward-vergent inactive thrust with syndeformational strata in basin bottom and postdeformational strata above. **c.** Sparker profile of wedge across active-inactive domain boundary. VE=4.90x within the sediments using a velocity of 1700 m/s. **d.** Map showing location of A-D, F-G. **e.** Sparker profile of wedge across active-inactive domain boundary. VE=2.48x within the sediments using a velocity of 1700 m/s. **f.** Detail of active domain basin from panel (d). Active late Quaternary fault cuts syndeformational strata. **g.** Detail of inactive domain basin from panel (d). Syndeformational strata showing folding separated from postdeformational strata by an unconformity.

is visible in a large coulee (Fig. 6a; described in Beeson et al., 2017). This frontal thrust is segmented at 46.4°N where the right-lateral offset on Fault E displaces the anticline seaward by 4 km. At the active-inactive domain boundary, two short, 9 km long inactive seaward-vergent faults are imaged.

We identify two, short (~14 km) incipient frontal

thrusts at 46.3°N forming 5 km seaward of the well-developed frontal thrust offset by Fault E (Fig. 6a). The seaward-vergent incipient thrust is cut by the more active landward-vergent incipient thrust, which produces a seafloor signature (Fig. 6c). Just south of 46.2°N, both incipient frontal thrusts as well as the previously dominant frontal thrust end as the deformation front steps

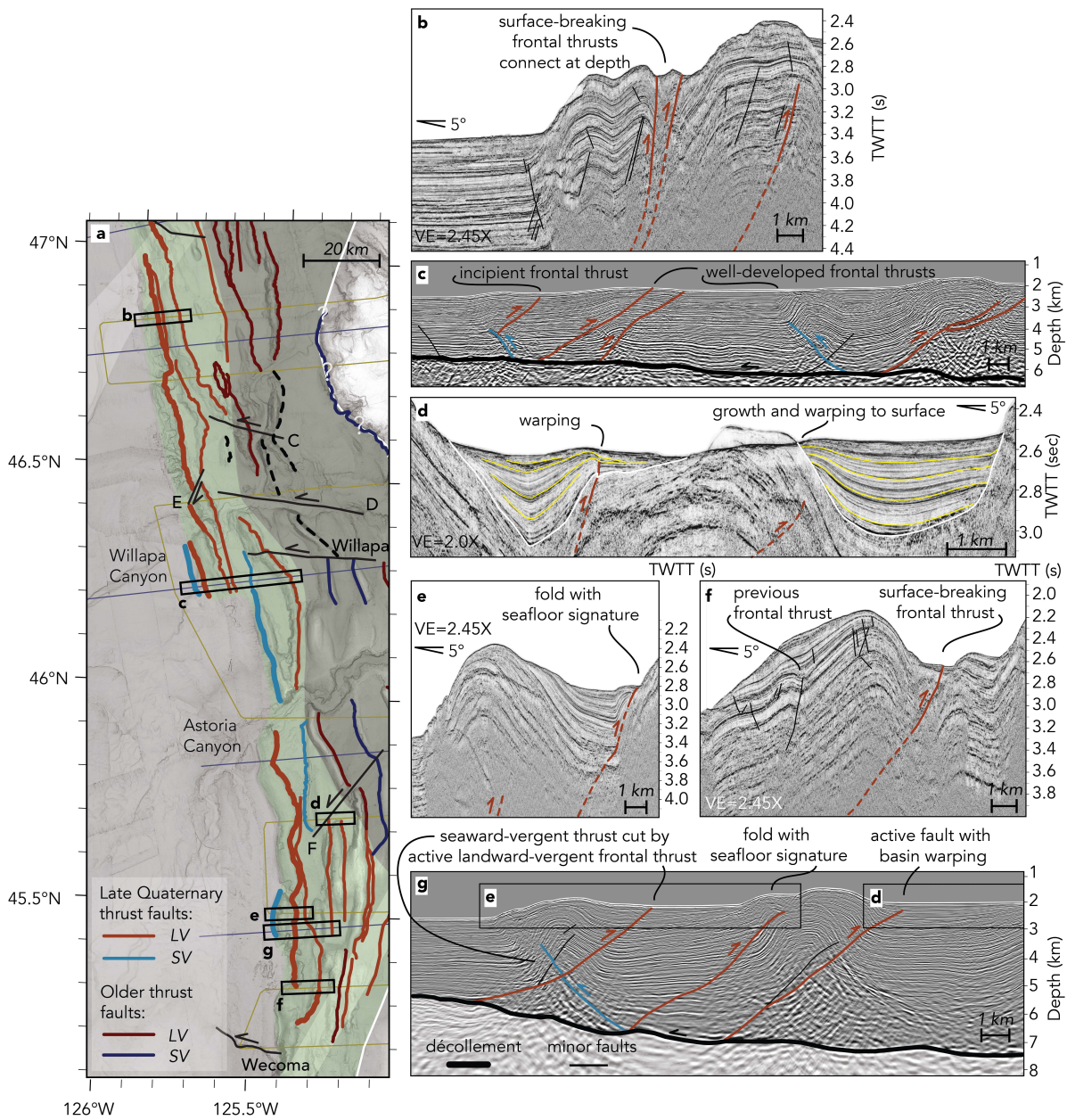


Figure 6 Characterization of the active domain along strike. Vertical exaggeration (VE) for all sparker profiles shown is 2.45x within the sediments using a velocity of 1700 m/s, except d which has a VE=2.0x **a.** Map showing the location of b-g. Late Quaternary active thrust faults which act as the frontal thrust in each location are highlighted with bold lines. **b.** Sparker profile. Doubly folded frontal anticline with two active surface-breaking landward-vergent thrusts with another fault-propagation fold imaged seaward. **c.** CASIE21 image. An incipient seaward-vergent frontal thrust is cut by an incipient landward-vergent frontal thrust. The well-developed frontal thrusts from north of this line (landward-vergent) and south of this line (seaward-vergent) are imaged. **d.** Sparker profile. Typical appearance of basins documenting late Quaternary faulting within the active domain. An active landward-vergent thrust is imaged in basin on left and another is inferred under anticline in middle of panel due to presence growth strata in basin nearby. **e.** Sparker profile. Frontal anticline controlled by a landward-vergent frontal thrust with an additional late Quaternary active frontal thrust creating a seafloor fold in the basin behind it. **f.** Sparker profile. Frontal anticline with surface-breaking frontal thrust. **g.** CASIE21 image showing location of basins in d and e. Westward active fault with seafloor warping shown in d appear in the right basin. Landward-vergent frontal thrust and second thrust with seafloor fold signature shown in e appear in the left basin.

landward by 15 km to a seaward-vergent thrust for a 32 km span, which decreases the width of the active domain from 22 km to 15 km. Both incipient frontal thrusts, the well-developed landward-vergent frontal thrust, and the seaward-vergent frontal thrust are imaged in Fig. 6c.

Between the Willapa Canyon Fault and Fault F, mixed vergence dominates both the active and inactive domains (Fig. 4). The width of the active domain is at its minimum value, around 15 km, when crossing Astoria Canyon, and begins to increase again to the south. Regularly spaced, 15 km wide thrust sheets with a smooth

sedimentary cover are typical in this area. Faults in basins which create seafloor folds or fault propagation fold anticlines with basinal growth strata to the surface remain common in this region (Fig. 6d).

South of Astoria Canyon, the deformation front is defined by a continuous landward-vergent frontal thrust 65 km in length (Fig. 6a). While this fault itself is deep-seated and not well-imaged in sparker data, sediment packages onlapping onto the frontal anticline indicate recent activity (Fig. 6d). This landward-vergent frontal thrust cuts a less active, shorter, 13 km long seaward-vergent thrust at the deformation front (Fig. 6f). Farther south at 45.3°N, the offset on this fault is smaller, so we classify it as a protothrust and do not extend it on the map. The second active fault at 45.5°N comes close to the seafloor, producing a large fold with a seafloor signature (Fig. 6d-f). This fault is the dominant frontal thrust at 45.3°N and produces a prominent 20 m seafloor scarp in this region (Fig. 6f).

From 45.5°N to 45.1°N, we observe active faulting to the inner-outer wedge boundary, so we extend the active domain to 40 km in width to encompass the entire outer wedge (Fig. 7a). Fault spacing decreases to 10 km and anticlines become more closely spaced and less distinct. Thinning and warping of the uppermost sediment package is observed above three active landward-vergent thrusts at 45.5°N (Fig. 7b). The westernmost active fault imaged in Fig. 7b has an 80 m high fold at the seafloor. Farther south, by 45.3°N, the typical geomorphic character of the LVZ is replaced by an uplifted plateau-like region without distinct anticlines. In this area, faulting to the surface is widespread (Fig. 7c). Onlapping sediment packages with no stratal thinning appear to the east of this active plateau, but they do not drape the uplifted zone, so it is uncertain whether the surface-reaching faults we image are active in this area. Regardless, we classify this area as active, though its features are much different from the active domain we observe in most of the LVZ.

4.3 The inactive domain

In the inactive domain, we identify 26 older Quaternary faults and three late Quaternary active faults, in addition to four inferred but not imaged thrusts. These faults exhibit lengths ranging from 5.4 to 64.2 km, with an average length of 25.1 km. The inactive domain fault strikes vary between 316° in the north and 345° in the south end of the LVZ. Landward vergence is observed for 21 of 29 imaged faults.

The inactive domain at the northern boundary of the LVZ at 48°N is approximately 20 km wide (Fig. 4). We map only two faults in this area which are traces of two seafloor anticlines near the active-inactive domain boundary. These faults are short, 19 and 26 km in length, and are not crossed by any seismic lines, so are mapped as inferred thrusts. The Juan de Fuca Canyon turns toward the north at 47.55°N, covering the inactive domain with channel deposits in this region and obscuring possible faults.

South of the Quillayute Channel, distinct anticlines reappear, and minimal channel deposits allow the map-

ping of many inactive faults in this region. Between 47.4°N and 46.7°N, there is a region of prominent older Quaternary landward-vergent thrusting. The faults here are closely spaced at approximately 4 km apart. We map 11 of these faults in this area, ranging from 11 to 55 km in length. Basins in this region show flat strata with no deformation in the uppermost several sediment packages, indicating no recent activity, with some examples of buried faults (Fig. 5b) and unconformities (Fig. 5g). Just south of Quinault Canyon is the widest point of the inactive domain at 41 km across.

South of Grays Canyon, the inactive domain decreases in width again to about 25 km wide (Fig. 8b). Channel deposits and wide line spacing limit imaging of deformation in this region, but we do identify two inferred thrust faults 29 and 15 km in length based on seafloor geomorphology (dashed black lines, Fig. 8b). Between Willapa Canyon and the southern boundary of the inactive domain, there is a zone of mixed vergence. Anticlines increase in number and have a consistent spacing of approximately 8 km separated by wide, flat basins. The strike-slip Willapa Canyon Fault marks another wide point of the inactive domain where it measures 41 km across. The sparker imaging does not capture the area between Willapa and Astoria Canyons, but we use the CASIE21 data to identify four older Quaternary faults here, two of which have seaward vergence. These faults appear discontinuous and do not cross to the south of Astoria Canyon.

In the southernmost section of the inactive domain, around 45.9°N, vergence of faults alternates and fault spacing is 7 km on average (Fig. 8b). There are four inactive landward-vergent and two inactive seaward-vergent thrusts imaged, ranging in length from 11 km to 64 km. The basin landward of the seaward-vergent thrust just south of Astoria Canyon shows growth strata at depth and flat-lying strata in the near-surface separated by at least one prominent unconformity (Fig. 8c), confirming that both faults underlying the anticlines adjacent to this basin and imaged in the CASIE data are inactive (Fig. 8f). Another nearby basin shows a similar decrease in the presence of growth strata from depth to surface, with little activity at present (Fig. 8e). These basins are typical of those imaged throughout the inactive domain.

Faults near the southern termination of the inactive domain also show larger differences in evidence of activity along strike (Fig. 8b). For instance, the anticline nearest to the inner-outer wedge boundary has two inactive landward-vergent branches while the main branch shows late Quaternary activity (Fig. 8b). An active splay from the middle of the main thrust has a seafloor anticline height of 160 m above the adjacent basin. Similarly, just south of strike-slip Fault F and near the active-inactive domain boundary, a structural high emerges where a landward-vergent thrust changes activity along strike from inactive to active at 45.65°N (Fig. 7a, 8b). We terminate the inactive domain at this latitude as active faults become common throughout the entire outer wedge to the inner-outer wedge transition.

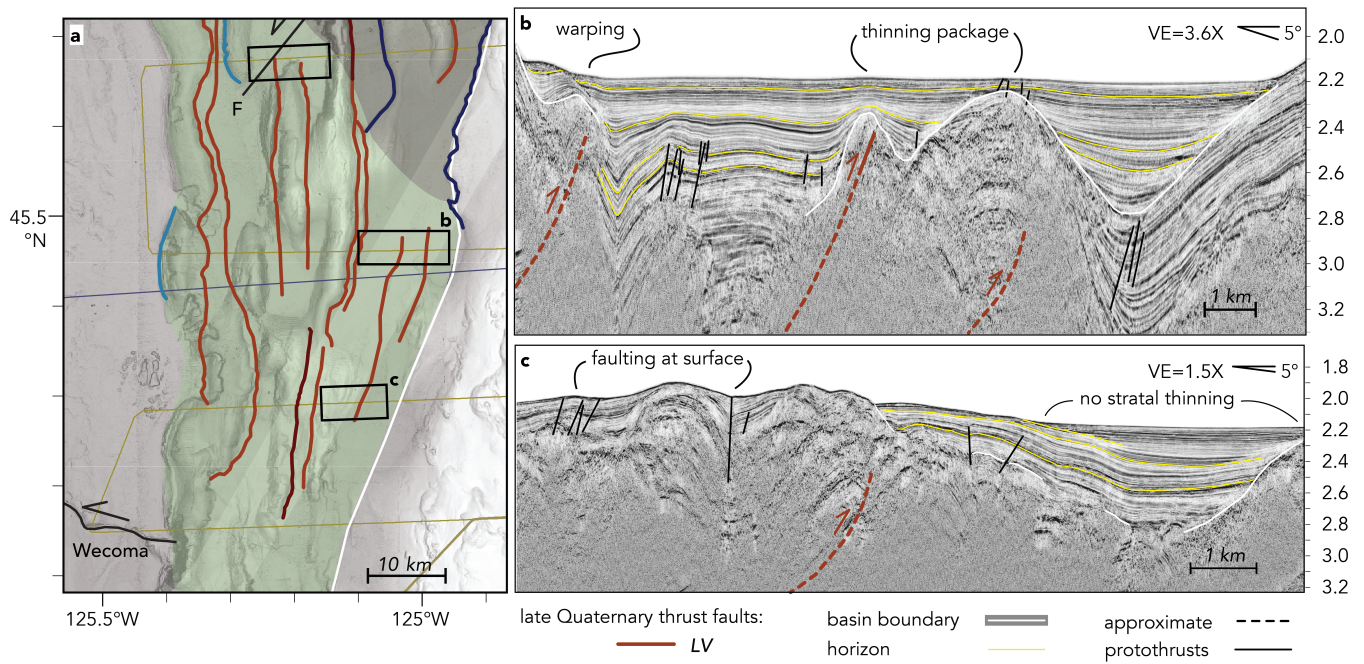


Figure 7 The southern portion of the active domain. **a.** Map showing location of b-c. **b.** Wide basin near landward edge of active domain showing near-surface deformation of youngest sediments. VE=3.64x within the sediments using a velocity of 1700 m/s. **c.** Complex active faulting imaged at surface. VE=1.46x within the sediments using a velocity of 1700 m/s.

4.4 The inner-outer wedge transition

Four seaward-vergent inactive faults are adjacent to or co-located with the inner-outer wedge boundary (Fig. 4). In the LVZ, we observe the presence of these faults in the CASIE21 data, but none show activity in the near-surface sparker data, indicating they are currently inactive. The northernmost fault associated with this boundary is at 47.5°N where an inactive, 21-km-long fault-propagation fold anticline crosses the boundary at a 19° strike. This strike direction is unique compared to the other faults we image located near the inner-outer wedge transition. In the basin to the west of this anticline, a short, 5 km inactive seaward-vergent thrust and a longer, 14 km active landward-vergent thrust are present.

A second seaward-vergent inactive thrust 13 km in length is located just south of Quinault Canyon (Fig. 8b). Like the remainder of the faults we discuss here, this thrust occurs at a slope angle that marks the inner-outer wedge transition. Similarly, a third imaged fault is located at the base of the slope between Grays and Willapa Canyons. This seaward-vergent thrust at the inner-outer wedge transition is longer at 43 km in length. Though this fault is clearly imaged in the CASIE21 data in this region, the sparker data do not image the fault itself (Fig. 8a). Rather, they capture the overlying sediments, which form a steep, non-depositional slope. The sedimentary package west of this slope documents the bending of strata at depth unconformably overlain by flat-lying sediment, indicating this region is no longer uplifting and the fault responsible for the older phase of basin deformation is no longer active. However, the fault imaged in the CASIE21 data appears to intersect the seafloor on a sloping surface that has no recent sed-

iment drape discernible in the sparker imagery. Therefore, we cannot rule out the possibility of recent fault activity along the CASIE21 structure.

The southernmost imaged fault, located south of Astoria Canyon, is the longest one associated with the inner-outer wedge transition in the LVZ, measuring 58 km in length. The basin to the west of the slope break shows growth and tilting at depth but decreasing activity to present (Fig. 8d). Similar to the previous examples, we consider this fault inactive.

4.5 Strike-slip faults

Strike-slip faults at a high oblique angle to the convergence direction cross-cut these zones of activity and may offset both active and inactive thrust fault structures. Strike-slip faults are inferred using bathymetry rather than in the seismic profiles, where oblique structures can be difficult to identify. In general, we observe strike-slip faults offsetting anticlinal ridges in the active and inactive domains resulting in the segmentation of thrust faults into shorter sections along strike. We identify 9 left-lateral and 1 right-lateral strike-slip faults, 7 of which strike west-northwest at 93° to 112° (Fig. 4). The remaining 2 faults strike northeast at nearly 90° to the predominant strike-slip fault orientation. Most of the strike-slip faults we map are located in the northern portion of the LVZ between the Juan de Fuca and Willapa Canyons, with two faults south of the Willapa Canyon Fault.

Fault A is 26 km in length and newly identified in this study based on the 2 km offset of the frontal thrust at 47.6°N. Fault B is coincident with an unnamed thrust fault in the Quaternary Faults Database (Schmitt, 2017) but we interpret the offset along this fault to be mostly

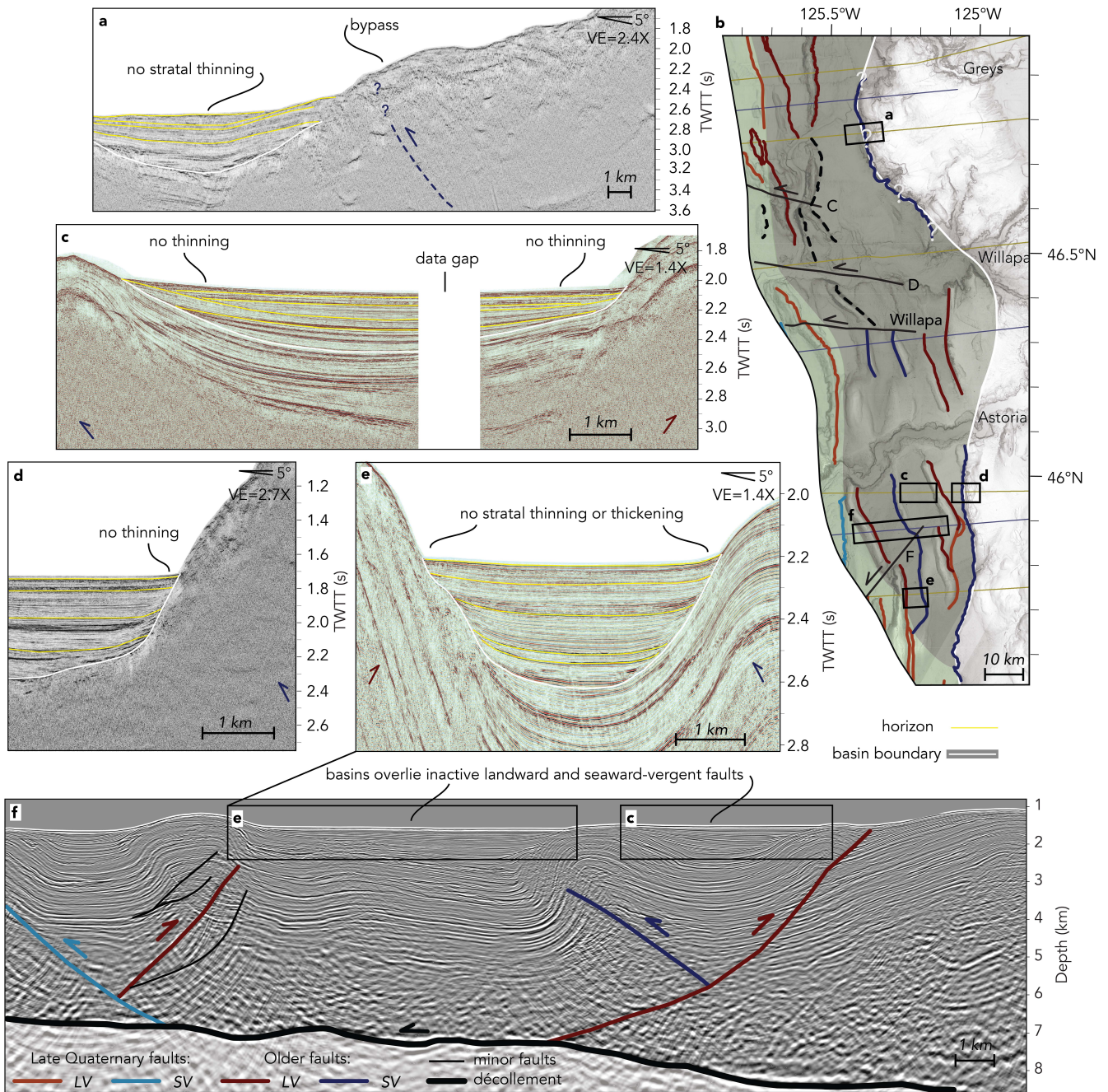


Figure 8 The inactive domain. Arrows without faults on annotated sparker profiles indicate the vergence of underlying faults which are not imaged in the sparker data but are imaged in the CASIE21 data. **a.** Sparker profile. Near-surface at location of inner-outer wedge transition showing flay-lying packages nearby. VE=2.40x within the sediments using a velocity of 1700 m/s. **b.** Map showing location of a, c-f. **c.** Sparker profile. Basin with flat-lying near-surface packages above a significant unconformity shows typical appearance of inactive domain basins. VE=1.40x within the sediments using a velocity of 1700 m/s. **d.** Sparker profile. Basin at inner-outer wedge transition showing inactivity of seaward-vergent thrust. VE=2.67x within the sediments using a velocity of 1700 m/s. **e.** Sparker profile. No present-day deformation on adjacent landward-vergent and seaward-vergent faults recorded in basin. VE=1.41x within the sediments using a velocity of 1700 m/s. **f.** CASIE21 image showing location of basins in e and c above inactive mixed vergence splay faults.

left-lateral due to the apparent offset of the two anticlines it crosses. The location of the North and South Nitinat Faults are slightly modified from representation of these faults in the Quaternary Faults Database (Schmitt, 2017) based on our analysis of the GMRT bathymetry in this study. The North Nitinat Fault crosses the frontal thrust, as well as two thrusts at the edge of the active domain, although not much offset of

these anticlines is observable on the seafloor. The South Nitinat Fault appears to offset the frontal thrust by 4 km at 47.05°N.

Faults C and D are newly identified left-lateral strike slip faults 20 and 42 km in length, respectively, based on the seafloor geomorphology of anticlines in this area and lineations present in the bathymetry (Fig. 4). Neither of these faults is present in the Quaternary Faults

Database (Schmitt, 2017) nor in the DOGAMI neotectonic map (Goldfinger et al., 2023). Fault E is modified in our study from initial observations by Beeson et al. (2017) and is the only right-lateral strike-slip fault in our map area. It offsets both the frontal and second anticlines by 2.5 km and has the highest apparent offset of any strike-slip fault in our study.

Just south of Fault D, the Willapa Canyon Fault is mapped at an updated location relative to the Quaternary Faults Database (Schmitt, 2017) due to observed offset along anticlines in both the active and inactive domain on the multibeam bathymetry. South of the Willapa Canyon Fault, there are only two additional strike-slip faults we identify (Fig. 4). Fault F is 28 km in length and is updated from an unnamed fault in the Quaternary Faults Database (Schmitt, 2017) based on its offset of several faults in the inactive domain. The southernmost strike-slip fault in our study area is the Wecoma Fault, whose location has been well-established by others (e.g., Appelgate et al., 1992; Tobin et al., 1993).

5 Discussion

We document widespread late Quaternary active faulting within the outermost, active domain of the outer wedge in the LVZ, and show that recent fault activity diminishes landward and is nearly nonexistent in the inactive domain. Based on the evidence we have presented above, we propose a conceptual model of Quaternary wedge evolution (Fig. 9) in which a concentrated zone of deformation spanning 3–4 individual thrusts and associated thrust sheets forms a continuously seaward-migrating zone of concurrent deformation 15 to 30 km wide; basins landward of this zone subsequently fill with thick sediment and fault activity subsides, creating a zone of no recent fault activity 20 to 40 km wide—the inactive domain.

5.1 Deformational domains and along-strike changes

We observe a major transition in outer wedge fault vergence and late Quaternary fault distribution occurring between 46.3°N and 45.5°N, separating the northern LVZ and the southern map area (Fig. 4). There is a transition at 46.3°N from predominantly landward vergence in the north to mixed vergence in the south. South of Astoria Canyon, the inactive domain decreases in width suddenly from 32 km at 46°N to 0 km at 45.5°N. The southernmost portion of our map area displays a different morphology from the rest of the LVZ, with the smallest outer wedge width and no region of widespread buried inactive faults (Fig. 7a). This contrast in outer wedge characteristics we document aligns with previous work that has designated a major along strike segmentation boundary at 46°N due to a change in the morphotectonic character of the accretionary wedge, such as a decrease in outer wedge width and an increase in outer wedge slope (Watt and Brothers, 2020). This leads us to conclude that the pattern of active and inactive domain faulting we propose here is restricted to the LVZ

between 48°N and 45.5°N and does not continue to the south of this area.

We detect only rare and spatially limited recent deformation associated with the inactive domain or in the inner-outer wedge transition. While there are seaward-vergent thrusts coincident with this boundary, notably the two faults between Grays and Astoria Canyons and the fault south of Astoria Canyon, analysis of the sparker seismic data indicates that deformation associated with these faults has decreased over time (Fig. 8a, 7c). Faults associated with this boundary may appear well-developed in crustal-scale seismic reflection data, indicating a large amount of cumulative slip, but such data sources lack the resolution to discriminate recent (i.e., late Quaternary) slip from longer timescale cumulative deformation. Our analysis suggests that faults at the inner-outer wedge transition in our map area have not experienced late Quaternary slip and thus are inactive at present.

While northwest-southeast oriented strike-slip faulting in this region has been well-documented (e.g., Appelgate et al., 1992; Han et al., 2018; McNeill et al., 1997; Goldfinger et al., 1996), there has been little investigation into the mechanics of faults oriented northeast-southwest, such as Fault E (Beeson et al., 2017) and Fault F. We note that these faults strike at the same orientation as propagator wakes in the downgoing plate (Nedimović et al., 2009), suggesting that strike-slip fault orientation may be influenced by lower plate topography (Fig. 4). Differential offset of anticlines along strike-slip faults may illuminate relative timing of fault formation. For example, the offset of the frontal thrust at Fault B (~0.5 km) is smaller compared to the offset of the second anticline thrust (~1.4 km), indicating that the frontal thrust is more recently formed in this region and there has been less time for strike-slip motion to offset it.

5.2 Uncertainties in mapping faults without age constraints

Because the morphology of active fault seafloor deformation depends on a variety of unknown factors, such as the integrated slip rate, the syntectonic sedimentation rate, and fault dip (Chiama et al., 2023), we have not distinguished between surface-breaking or buried active faults. However, we note cases of fault scarps with discrete surface offset, which definitively indicates Holocene and likely coseismic activity (McCalpin and Nelson, 2009). Three faults meet this criterion, all of which are located at the deformation front (Fig. 6b, e). The remaining faults in the active domain often produce seafloor fault signatures, but their fault tips do not reach the surface with displacement more than the vertical resolution of the sparker data (<3.75 m). This difference is likely because the frontal thrust faults are more recently formed rather than a difference in recency of activity between late Quaternary faults. Additionally, slope basin sediments are composed largely of turbidites and debris flows derived from adjacent anticlines and thus sedimentation rates are dominated by local, non-average effects and may vary widely between individual basins (Barnard, 1978; McAdoo et al.,

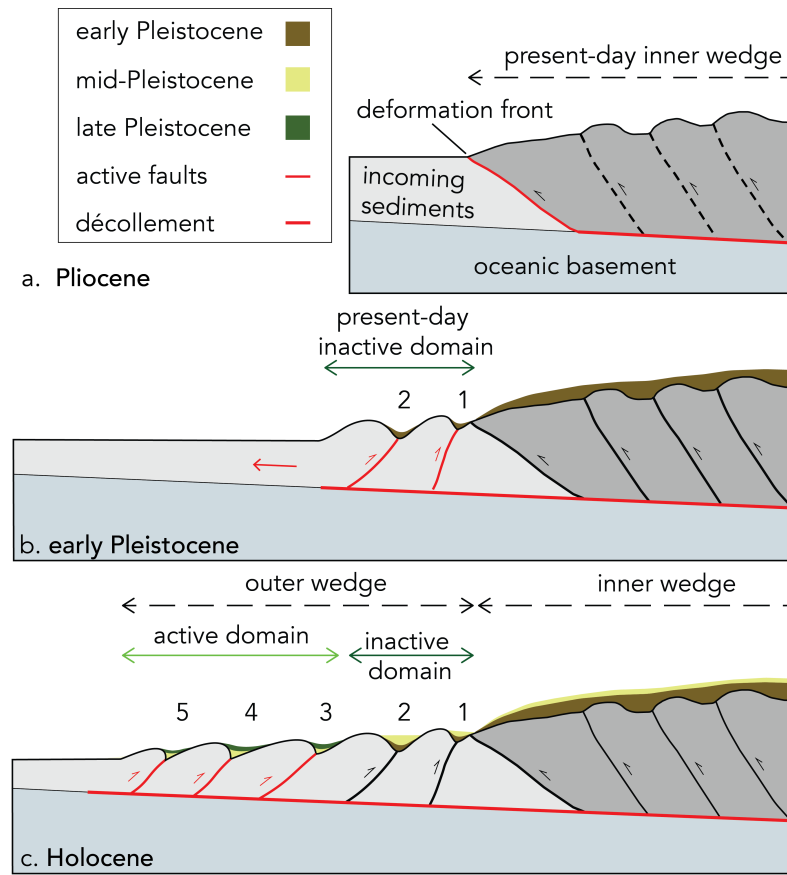


Figure 9 Conceptual model of wedge evolution. **a.** In the Pliocene, the present-day inner wedge composed the entire accretionary wedge in the LVZ. **b.** Quaternary glaciation begins at the beginning of the Pleistocene 2.58 Ma increasing the sedimentation rate and causing the outer wedge to build seaward continuously. The present-day inactive domain (basins 1-2) hosts active faults. **c.** Active domain basins 3-5 are formed and inactive domain basins 1-2 become inactive. Fault activity in the active domain continues today.

1997), as well as by the availability of accommodation space within each basin. This variability prevented us from identifying any reflectors which correlate across basins. The confounding effect of variable sedimentation rate means that we cannot quantitatively determine slip rates nor per-event displacements for specific faults without widespread coring and age dating of individual slope basins.

5.3 Conceptual model of wedge evolution during the Quaternary

The Cascadia subduction zone, particularly the LVZ, is known for its thick supra-wedge sedimentary cover among subduction zones worldwide. Sediment supply and accumulation rates are heavily influenced by climatic factors such as ice ages; for example, heavy sedimentation during the last glacial period, which ended approximately 11,000 years ago, extensively flooded the accretionary wedge in this region (Barnard, 1978; Underwood, 2002). Glaciation extended to the Juan de Fuca Strait, but glacially derived sediments were deposited largely between the Juan de Fuca and Astoria Canyons (Booth et al., 2003; Hill et al., 2022; Riedel et al., 2018).

Heavy wedge-top sedimentation has been shown to

influence accretionary wedge evolution and mechanics. Mechanical modeling indicates that high hinterland sediment input can produce widely spaced thrust sheets with low surface slope (Simpson, 2010), similar to the morphology of the LVZ at Cascadia. Specifically, high slope basin sedimentation tends to suppress underlying fault activity (Fuller et al., 2006), so that deformation either migrates outside of the sedimentation zone or resumes after sediment rate decreases by reactivating or forming out-of-sequence thrusts to reattain critical taper (Mannu et al., 2016, 2017).

Based on these previous findings and our results here, we present a conceptual model of wedge evolution for the LVZ during the Quaternary (Fig. 9). At the end of the Pliocene, the entire accretionary wedge consisted of the present-day inner wedge (Fig. 9a). At the ~2.58 Ma onset of Pleistocene glaciation, the accretionary wedge began to grow seaward by actively forming the now-inactive domain of the outer wedge through the formation of dominantly landward-vergent faults (Fig. 9a; e.g., Adam et al., 2004). Deformation during this time was widespread in the present-day inactive domain, and syndeformational strata were deposited in basins 1 and 2 (Fig. 9b). Heavy glacially induced sedimentation caused the deformation front to step seaward rapidly

and continuously during the Pleistocene, creating the entire present-day outer wedge (basins 3-5). As deformation migrated outward, faults deactivated in basins 1 and 2 and were buried by thick postdeformational strata (Fig. 9c). Deposition of these strata into forearc basins “turns off” the underlying faults, forcing migration of the active domain seaward (Fuller et al., 2006; Mannu et al., 2017; Simpson, 2010). We posit that an active domain consisting of the deformation front accompanied by a ~30 km region of active faulting therefore steps seaward continually over time, with faults trailing behind this zone becoming largely inactive. Our documentation of multiple incipient frontal thrusts and surface-breaking scarps at the deformation front suggests that this process is ongoing (e.g., Fig. 6b, c, e).

The outer wedge changes character south of Astoria Canyon because glacial sedimentation largely was deposited to its north (Booth et al., 2003; Riedel et al., 2018), and Holocene sedimentation has also been markedly lower south of Willapa Canyon (Barnard, 1978). We posit that the comparatively lower sediment input in our southernmost map area caused the deformation front to step seaward less significantly than in the rest of the LVZ and thus did not create an inactive domain in this region. Basins in the present-day outer wedge were likely not buried as completely and fault activity did not entirely deactivate as in the inactive domain elsewhere, instead remaining active throughout the Pleistocene (Fig. 7c, d).

Our conceptual model argues that rapid wedge-top sedimentation is the main control on atypical morphology and distribution of fault activity of the LVZ at Cascadia, and the key role of sediments in controlling wedge morphology is bolstered by similar observations at other sediment-rich subduction zones and modeling work based on critical wedge theory (e.g., Mannu et al., 2016; Simpson, 2010). For example, fault activity mapping at Makran—which has both high sediment thickness on the incoming plate as well as a high hinterland sediment supply—identified a belt of continuously active seaward-vergent faults close to the deformation front, with activity diminishing landward (Smith et al., 2012), similar to the pattern of landward-vergent faults we document at Cascadia. Along-strike morphotectonic changes at Sumatra are linked with variability in incoming sediment thickness, and the location of landward vergence is correlated with the highest sediment input (McNeill and Henstock, 2014), analogous to the Cascadia case. Wedges with a high hinterland sediment input and which exhibit low taper are supercritical, rather than subcritical, but still stable (Simpson, 2010). This can be ascribed to an increase in vertical stress which in turn reduces differential stress and renders fault slip unfavorable (Simpson, 2010).

5.4 Implications for megathrust rupture and tsunami generation

Recent large megathrust events have highlighted the potential for shallow fault slip, both along the décollement and on splay faults within the accretionary wedge. For example, seismic and geological work has estab-

lished that two splay faults slipped coseismically during the 1964 M_w 9.2 Alaska earthquake (Liberty et al., 2013; Plafker, 1969). Seafloor scarps documented shortly after the 2004 M_w 9.1 Sumatra earthquake indicate that wedge faults either slipped coseismically, or bending moment faulting occurred while the décollement slipped below them (Henstock et al., 2006). Fault scarps at the deformation front created by the M_w 9.1 2011 Tohoku-Oki earthquake have been identified and calculations suggest that up to 120 m of slip was accommodated (Ueda et al., 2023).

In this work, we have documented near-surface late Pleistocene to Holocene deformation on numerous splay faults offshore Washington and northern Oregon, and previous studies using lower-resolution seismic reflection data have shown that displacement at depth amounts to kilometers of slip (e.g., Adam et al., 2004; MacKay, 1995; Booth-Rea et al., 2008). The observed displacement on active faults in the outer wedge must be formed by either (a) continuous steady creep, (b) rapid coseismic slip, (c) afterslip immediately following a large rupture, or (d) some combination of these processes. The accretionary wedge in this region is known to be either strongly geodetically locked or lying in a stress shadow zone; either way, it is accumulating slip deficit rather than steadily creeping (Lindsey et al., 2021).

Discriminating between slow steady creep during the interseismic period and rapid coseismic slip and afterslip during megathrust rupture in sparker seismic reflection profiles is difficult and likely requires combined detailed bathymetric and structural analysis based on even higher resolution imaging (e.g. AUV bathymetry and chirp). Limited other studies have documented that afterslip may represent 20% to 50% of the documented total slip for megathrust events, the remainder of which is coseismic (e.g., Brooks et al., 2023; Lin et al., 2013). This implies that even if some of the offset visible on seismic data is due to afterslip, at least a portion to a majority of the accumulated slip on each fault is coseismic in nature. Considering these lines of reasoning, we therefore conclude that a large portion of the active domain deformation we show here is likely rapid, coseismic slip that produces seafloor displacement and therefore uplift during megathrust earthquakes. The discrete surface scarps with brittle offset that we document here (e.g., Fig. 6b, f) are categorically considered evidence of coseismic slip in terrestrial environments (e.g., Chiama et al., 2023), but even seafloor fold scarps we show would be geomorphic evidence for surface-rupturing earthquakes, and would be sites chosen for paleoseismic investigation were they on land (e.g., McCalpin and Nelson, 2009).

An additional argument favoring coseismic rapid slip events on these splays is that the frictional conditions for shallow slip are met at Cascadia due to the thick sediment cover and young age of the subducting plate. The 100-150°C threshold at which a variety of low-grade metamorphic processes occur is thought to correspond to the minimum temperature for earthquake nucleation at subduction zones (Hyndman and Wang, 1993; Moore and Saffer, 2001). This condition is met at Cascadia

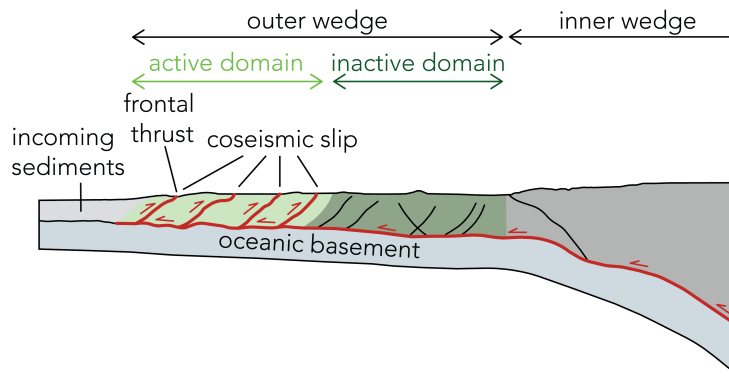


Figure 10 Proposed model of coseismic slip in the LVZ during megathrust events. The décollement hosts large slip to the toe of the accretionary wedge, inducing slip on the frontal thrust and other splay faults in the active domain (colored red). The inactive domain faults, including at the inner-outer wedge boundary, do not slip, and the displacement is efficiently transferred up the megathrust to the toe region.

above the plate interface and within the accretionary wedge sediments, suggesting that shallow seismogenic behavior on the megathrust and splay faults is possible (Salmi et al., 2017). Recent thermal modeling at Sumatra suggests that shallow diagenetic strengthening of wedge sediments prior to the deformation front due to thick sedimentary cover played a role in driving shallow slip during the 2004 M_w 9.1 event (Hüpers et al., 2017; Stevens et al., 2021). At Nankai, core samples documenting frictional heating of shallow sediments from coseismic slip along the megathrust and megasplay faults confirm that shallow slip in accretionary wedges is possible (Sakaguchi et al., 2011; Yamaguchi et al., 2011). Earthquakes may in any case slip into shallow regions below the 100–150°C threshold due to dynamic overshoot, as was likely seen in the 2011 Tohoku-Oki earthquake (e.g. Ide et al., 2011; Sun et al., 2017).

In the past, backward rupture branching was perceived to be improbable, so rupture propagation between faults connected at acute angles was not considered. However, dynamic modeling has found that slip on the megathrust can activate multiple seaward or landward-vergent accretionary wedge faults through dynamic triggering (van Zelst et al., 2022; Xu et al., 2015). Additionally, during the 2023 M_w 7.8 Kahramanmaraş earthquake, bilateral rupture propagated onto faults with variable dips and onto a splay fault through an acute fault bend likely due to a cascading dynamic rupture process, rather than direct triggering (Ding et al., 2023).

While identified active faults in map view are segmented along strike into ~30 km sections on average, it is possible that they would rupture together along strike and in concert with the décollement during large megathrust events. Multiple lines of reasoning suggest these faults would not rupture alone and produce their own earthquakes independent of the megathrust, including: they are in the stress shadow of a locked megathrust (e.g., Lindsey et al., 2021); faults in compliant sediments are not strong enough to initiate coseismic rupture; and very little microseismicity is recorded

in this region (e.g., Stone et al., 2018; Morton et al., 2023). There are documented examples of destructive earthquakes in fold-and-thrust belts on land or in subduction zone settings with simultaneous rupture of multiple, separate faults, and/or surface fault rupture on out-of-sequence faults. The 2016 M_w 7.8 Kaikoura earthquake saw rupture of at least 20 interconnected strike-slip and thrust faults with a maximum surface displacement of 12 meters and caused a local tsunami (Kaiser et al., 2017; Litchfield et al., 2018), possibly linked by an underlying décollement fault (Ulrich et al., 2019). The 2008 M_w 7.9 Wenchuan earthquake ruptured at least one out-of-sequence fault while no displacement was recorded on the frontal thrust or other major thrusts in the Longmen Shan fold-and-thrust belt (Hubbard and Shaw, 2009). We suggest future Cascadia megathrust events could similarly involve complex rupture of many splay faults in the outer wedge.

Tsunami excitation by splay faults depends on fault dip, length, and slip magnitude (Wendt et al., 2009). Splay faults imaged in this study are often listric and increase in dip in the near surface, with some approaching vertical as they intersect the seafloor. Similar high-angle near-surface splay faults have been observed using sparker seismic reflection data at other subduction zones, including the Cape Cleare and Patton Bay Faults in the Alaska subduction zone, with 70° dip in the near-surface and up to 39 m-high seafloor scarps (Liberty et al., 2013), but 30–40° dip overall down to 20 km below the surface (Haeussler et al., 2015). Faults with steeper near-surface dips have more potential for tsunami excitation because of greater vertical seafloor displacement (e.g., Qiu and Barbot, 2022). Models that have included splay fault rupture at Cascadia have shown that splay fault rupture can double median tsunami height compared to megathrust-only fault rupture (Aslam et al., 2021).

Modeling has shown that the tsunami from the 1700 Cascadia event can be reproduced in Japan by a minimum of an M_w 8.7 rupture, and that such a tsunami would require a minimum fault source length of only

400 km to be created (Melgar, 2021; Satake et al., 1996). Since there is evidence that splay faults like those documented here may be able to rupture together with the megathrust, linking along strike to create longer rupture lengths, it follows that activation of multiple separate strands of landward-vergent splay faults could contribute to both far-field and local tsunami signal during a megathrust event. We support the inclusion of landward-vergent splay fault rupture in future tsunami scenario models.

Megathrust earthquakes that ruptured splay faults like the Alaska 1964 M_w 9.2, and as suggested for the Tonankai 1944 M_w 8.0 event, have involved long faults located at the inner-outer wedge transition (Moore et al., 2007; von Huene et al., 2021), sometimes called “megaspays” (Tobin and Kinoshita, 2006). Because of this, tsunami scenario models that incorporate splay faulting in Cascadia have used a margin-long splay fault located at that boundary (Gao et al., 2018; Witter et al., 2013). We identify only isolated, inactive faults at the inner-outer wedge transition. Our analysis suggests that activation of and slip on landward-vergent splay faults and their associated anticlines in the active domain of the outer wedge is more likely than that of inner-outer wedge boundary-related splay faults.

To synthesize these observations and considerations derived from wedge mechanics, we infer that our results are therefore consistent with a syn-rupture scenario in which the inner wedge and the inactive part of the outer wedge all act as a dominantly rigid upper plate block, translating seaward during megathrust slip without splay activation (Fig. 10). The large (potentially 10s of meters) of slip is transferred up the megathrust and distributed onto one to—more likely—several splay thrusts in the outermost, active domain, thereby creating enhanced seafloor displacement and multiple branch rupture over a 15–30 km width of the shallowest portion of the wedge (Fig. 10). Our results favor seafloor deformation of not the frontal thrust alone, but rather the entire active domain.

6 Conclusions

Using a combination of high-resolution near-surface and lower-resolution crustal-scale seismic reflection data and multibeam bathymetry, we identify and map splay faults in the outer wedge of the landward vergence zone of the Cascadia accretionary wedge over a region spanning ~400 km along strike of the largest geodetically locked portion of the megathrust. By conducting stratigraphic analysis of slope basins in the outer wedge, we determine recency of activity of splay faults. We identify two regions of the outer wedge: the active domain, spanning the region within ~30 km landward of the deformation front, which contains predominantly recently active landward-vergent splay faults; and the inactive domain, located between the active domain and the inner-outer wedge transition, which contains dominantly inactive, buried landward-vergent splay faults. We develop a conceptual model of continuous seaward migration of a ~30 km active deformation zone including the deformation front and sev-

eral anticlines landward. Based on these results, we infer that, in megathrust events at Cascadia, complex outer wedge deformation including rupture on multiple splay faults is favored, and that slip is strongly partitioned to the active domain of the outer wedge. The potential of slip on multiple, simultaneously activated landward-vergent splay faults close to the deformation front should be accounted for in future tsunami hazard modeling scenarios.

Acknowledgements

Funding for this work was provided by the U.S. Geological Survey Coastal and Marine Hazards and Resources Program, the University of Washington, and the U.S. National Science Foundation through awards 2103713 and 2217468 to Tobin. We thank all of the individuals involved with collection and processing of high-resolution sparker seismic-reflection data, specifically Emily Roland, Jared Kluesner, and Alicia Balster-Gee, as well as the CASIE21 data, including Suzanne Carbotte, Shuoshuo Han, Brian Boston, and Jeff Beeson. Any use of trade, product, or firm names is for descriptive purposes only and does not imply endorsement by the U.S. Government. James Conrad provided comments on an early version of the manuscript. The manuscript was greatly improved by reviews from Lisa McNeill and Utsav Mannu.

Data and code availability

The seismic data utilized in this study are publicly available. The high-resolution multi-channel sparker seismic data can be found as a USGS data release (Balster-Gee et al., 2023, USGS field activity 2019-024-FA). The CASIE21 multi-channel seismic reflection data are hosted on Marine Geoscience Data System (Carbotte et al., 2023). Seismic interpretation was conducted using the *Kingdom Suite*.

Competing interests

The authors have no competing interests.

References

- Adam, J., Klaeschen, D., Kukowski, N., and Flueh, E. Upward delamination of Cascadia Basin sediment infill with landward frontal accretion thrusting caused by rapid glacial age material flux. *Tectonics*, 23(3), June 2004. doi: 10.1029/2002tc001475.
- Appelgate, B., Goldfinger, C., MacKay, M. E., Kulm, L. D., Fox, C. G., Embley, R. W., and Meis, P. J. A left-lateral strike-slip fault seaward of the Oregon Convergent Margin. *Tectonics*, 11(3): 465–477, June 1992. doi: 10.1029/91tc02906.
- Aslam, K. S., Thomas, A. M., and Melgar, D. The Effect of Fore-Arc Deformation on Shallow Earthquake Rupture Behavior in the Cascadia Subduction Zone. *Geophysical Research Letters*, 48 (20), Oct. 2021. doi: 10.1029/2021gl093941.
- Balster-Gee, A. F., Miller, N. C., Watt, J. T., Roland, E. C., Kluesner, J. W., Heller, S. J., Hart, P. E., Sliter, R. W., Myers, E. K., Wyland, R. M., Marcuson, R. K., Johnson, C., Nichols, A. R., Pszczola, K.,

- and Williams, C. High-resolution multichannel sparker seismic-reflection and chirp sub-bottom data acquired along the Cascadia margin during USGS field activity 2019-024-FA, 2023. doi: 10.5066/P96ZBXK8.
- Barnard, W. D. The Washington continental slope: Quaternary tectonics and sedimentation. *Marine Geology*, 27(1-2):79–114, May 1978. doi: 10.1016/0025-3227(78)90075-0.
- Beeson, J. W., Goldfinger, C., and Fortin, W. F. Large-scale modification of submarine geomorphic features on the Cascadia accretionary wedge caused by catastrophic flooding events. *Geosphere*, 13(5):1713–1728, July 2017. doi: 10.1130/ges01388.1.
- Bilotti, F. and Shaw, J. H. Deep-water Niger Delta fold and thrust belt modeled as a critical-taper wedge: The influence of elevated basal fluid pressure on structural styles. *AAPG Bulletin*, 89(11):1475–1491, Nov. 2005. doi: 10.1306/06130505002.
- Booth, D. B., Troost, K. G., Clague, J. J., and Waitt, R. B. *The Cordilleran Ice Sheet*, page 17–43. Elsevier, 2003. doi: 10.1016/s1571-0866(03)01002-9.
- Booth-Rea, G., Klaeschen, D., Grevemeyer, I., and Reston, T. Heterogeneous deformation in the Cascadia convergent margin and its relation to thermal gradient. *Tectonics*, 27(4), July 2008. doi: 10.1029/2007tc002209.
- Brooks, B. A., Goldberg, D., DeSanto, J., Ericksen, T. L., Webb, S. C., Nooner, S. L., Chadwell, C. D., Foster, J., Minson, S., Witter, R., Haeussler, P., Freymueller, J., Barnhart, W., and Nevitt, J. Rapid shallow megathrust afterslip from the 2021 M8.2 Chignik, Alaska earthquake revealed by seafloor geodesy. *Science Advances*, 9(17), Apr. 2023. doi: 10.1126/sciadv.adf9299.
- Byrne, D. E., Davis, D. M., and Sykes, L. R. Loci and maximum size of thrust earthquakes and the mechanics of the shallow region of subduction zones. *Tectonics*, 7(4):833–857, Aug. 1988. doi: 10.1029/tc007i004p00833.
- Carbotte, S., Han, S., Boston, B., and Canales, J. Processed pre-stack depth-migrated seismic reflection data from the 2021 CASIE21 multi-channel seismic survey (MGL2104), 2023. doi: 10.26022/IEDA/331274.
- Calet, J. *Proceedings of the Ocean Drilling Program, 146 Part 1 Scientific Results*. Ocean Drilling Program, Dec. 1995. doi: 10.2973/odp.proc.sr.146-1.1995.
- Chiama, K., Chauvin, B., Plesch, A., Moss, R., and Shaw, J. H. Geomechanical Modeling of Ground Surface Deformation Associated with Thrust and Reverse-Fault Earthquakes: A Distinct Element Approach. *Bulletin of the Seismological Society of America*, 113(4):1702–1723, Apr. 2023. doi: 10.1785/0120220264.
- Davis, D., Suppe, J., and Dahlen, F. A. Mechanics of fold-and-thrust belts and accretionary wedges. *Journal of Geophysical Research: Solid Earth*, 88(B2):1153–1172, Feb. 1983. doi: 10.1029/jb088ib02p01153.
- DeMets, C., Gordon, R. G., and Argus, D. F. Geologically current plate motions. *Geophysical Journal International*, 181(1):1–80, Apr. 2010. doi: 10.1111/j.1365-246x.2009.04491.x.
- Ding, X., Xu, S., Xie, Y., Van den Ende, M., Premus, J., and Ampuero, J.-P. The sharp turn: Backward rupture branching during the 2023 Mw 7.8 Kahramanmaraş (Türkiye) earthquake. *Seismica*, 2(3), Nov. 2023. doi: 10.26443/seismica.v2i3.1083.
- Fisher, M. A., Flueh, E. R., Scholl, D. W., Parsons, T., Wells, R. E., Trehu, A., Brink, U. t., and Weaver, C. S. Geologic processes of accretion in the Cascadiasubduction zone west of Washington State. *Journal of Geodynamics*, 27(3):277–288, Feb. 1999. doi: 10.1016/s0264-3707(98)00001-5.
- Flueh, E. R., Fisher, M. A., Bialas, J., Childs, J. R., Klaeschen, D., Kukowski, N., Parsons, T., Scholl, D. W., ten Brink, U., Tréhu, A. M., and Vidal, N. New seismic images of the Cascadia subduction zone from cruise SO108 — ORWELL. *Tectonophysics*, 293(1-2):69–84, July 1998. doi: 10.1016/s0040-1951(98)00091-2.
- Frederik, M. C. G., Gulick, S. P. S., Austin, J. A., Bangs, N. L. B., and Udrek. What 2-D multichannel seismic and multibeam bathymetric data tell us about the North Sumatra wedge structure and coseismic response. *Tectonics*, 34(9):1910–1926, Sept. 2015. doi: 10.1002/2014tc003614.
- Fujiwara, T., Kodaira, S., No, T., Kaiho, Y., Takahashi, N., and Kaneda, Y. The 2011 Tohoku-Oki Earthquake: Displacement Reaching the Trench Axis. *Science*, 334(6060):1240–1240, Dec. 2011. doi: 10.1126/science.1211554.
- Fuller, C. W., Willett, S. D., and Brandon, M. T. Formation of forearc basins and their influence on subduction zone earthquakes. *Geology*, 34(2):65, 2006. doi: 10.1130/g21828.1.
- Gao, D., Wang, K., Insua, T. L., Sypus, M., Riedel, M., and Sun, T. Defining megathrust tsunami source scenarios for northernmost Cascadia. *Natural Hazards*, 94(1):445–469, July 2018. doi: 10.1007/s11069-018-3397-6.
- Goldfinger, C., Kulm, L. D., Yeats, R. S., Appelgate, B., MacKay, M. E., and Moore, G. F. Transverse structural trends along the Oregon convergent margin: Implications for Cascadia earthquake potential and crustal rotations. *Geology*, 20(2):141, 1992. doi: 10.1130/0091-7613(1992)020<0141:tstato>2.3.co;2.
- Goldfinger, C., Kulm, L. D., Yeats, R. S., Hummon, C., Huftile, G. J., Niem, A. R., and McNeill, L. C. *Oblique Strike-Slip Faulting of the Cascadia Submarine Forearc: The Daisy Bank Fault Zone off Central Oregon*, page 65–74. American Geophysical Union, Mar. 1996. doi: 10.1029/gm096p0065.
- Goldfinger, C., Kulm, L. D., Yeats, R. S., McNeill, L., and Hummon, C. Oblique strike-slip faulting of the central Cascadia submarine forearc. *Journal of Geophysical Research: Solid Earth*, 102(B4): 8217–8243, Apr. 1997. doi: 10.1029/96jb02655.
- Goldfinger, C., Beeson, J., Romsos, C., and Patton, J. Neotectonic Map of the Cascadia Margin. (open-file report o-23-05), Oregon Department of Geology and Mineral Industries, 2023.
- Gulick, S. P., Bangs, N. L., Moore, G. F., Ashi, J., Martin, K. M., Sawyer, D. S., Tobin, H. J., Kuramoto, S., and Taira, A. Rapid forearc basin uplift and megasplay fault development from 3D seismic images of Nankai Margin off Kii Peninsula, Japan. *Earth and Planetary Science Letters*, 300(1-2):55–62, Nov. 2010. doi: 10.1016/j.epsl.2010.09.034.
- Gulick, S. P. S., Austin, J. A., McNeill, L. C., Bangs, N. L. B., Martin, K. M., Henstock, T. J., Bull, J. M., Dean, S., Djajadihardja, Y. S., and Permana, H. Updip rupture of the 2004 Sumatra earthquake extended by thick indurated sediments. *Nature Geoscience*, 4(7):453–456, June 2011. doi: 10.1038/ngeo1176.
- Gutscher, M.-A., Klaeschen, D., Flueh, E., and Malavieille, J. Non-Coulomb wedges, wrong-way thrusting, and natural hazards in Cascadia. *Geology*, 29(5):379, 2001. doi: 10.1130/0091-7613(2001)029<0379:ncwwwt>2.0.co;2.
- Haeussler, P. J., Armstrong, P. A., Liberty, L. M., Ferguson, K. M., Finn, S. P., Arkle, J. C., and Pratt, T. L. Focused exhumation along megathrust splay faults in Prince William Sound, Alaska. *Quaternary Science Reviews*, 113:8–22, Apr. 2015. doi: 10.1016/j.quas-cirev.2014.10.013.
- Han, S., Carbotte, S. M., Canales, J. P., Nedimović, M. R., and Carton, H. Along-Trench Structural Variations of the Subducting Juan de Fuca Plate From Multichannel Seismic Reflection Imaging. *Journal of Geophysical Research: Solid Earth*, 123(4): 3122–3146, Apr. 2018. doi: 10.1002/2017jb015059.
- Henstock, T. J., McNeill, L. C., and Tappin, D. R. Seafloor morphology of the Sumatran subduction zone: Surface rupture during megathrust earthquakes? *Geology*, 34(6):485, 2006. doi: 10.1130/22426.1.

- Hill, J. C., Brothers, D. S., Craig, B. K., ten Brink, U. S., Chaytor, J. D., and Flores, C. H. Geologic controls on submarine slope failure along the central U.S. Atlantic margin: Insights from the Currituck Slide Complex. *Marine Geology*, 385:114–130, Mar. 2017. doi: 10.1016/j.margeo.2016.10.007.
- Hill, J. C., Watt, J. T., and Brothers, D. S. Mass wasting along the Cascadia subduction zone: Implications for abyssal turbidite sources and the earthquake record. *Earth and Planetary Science Letters*, 597:117797, Nov. 2022. doi: 10.1016/j.epsl.2022.117797.
- Hubbard, J. and Shaw, J. H. Uplift of the Longmen Shan and Tibetan plateau, and the 2008 Wenchuan ($M = 7.9$) earthquake. *Nature*, 458(7235):194–197, Mar. 2009. doi: 10.1038/nature07837.
- Hyndman, R. D. and Wang, K. Thermal constraints on the zone of major thrust earthquake failure: The Cascadia Subduction Zone. *Journal of Geophysical Research: Solid Earth*, 98(B2): 2039–2060, Feb. 1993. doi: 10.1029/92jb02279.
- Hüpers, A., Torres, M. E., Owari, S., McNeill, L. C., Dugan, B., Henstock, T. J., Milliken, K. L., Petronotis, K. E., Backman, J., Bourlange, S., Chemale, F., Chen, W., Colson, T. A., Frederik, M. C. G., Guèrin, G., Hamahashi, M., House, B. M., Jeppson, T. N., Kachovich, S., Kenigsberg, A. R., Kuranaga, M., Kutterolf, S., Mitchison, F. L., Mukoyoshi, H., Nair, N., Pickering, K. T., Poudroux, H. F. A., Shan, Y., Song, I., Vannucchi, P., Vrolijk, P. J., Yang, T., and Zhao, X. Release of mineral-bound water prior to subduction tied to shallow seismogenic slip off Sumatra. *Science*, 356(6340):841–844, May 2017. doi: 10.1126/science.aal3429.
- Ide, S., Baltay, A., and Beroza, G. C. Shallow Dynamic Overshoot and Energetic Deep Rupture in the 2011 Mw 9.0 Tohoku-Oki Earthquake. *Science*, 332(6036):1426–1429, June 2011. doi: 10.1126/science.1207020.
- Ishii, M., Shearer, P. M., Houston, H., and Vidale, J. E. Extent, duration and speed of the 2004 Sumatra–Andaman earthquake imaged by the Hi-Net array. *Nature*, 435(7044):933–936, June 2005. doi: 10.1038/nature03675.
- Ito, Y., Tsuji, T., Osada, Y., Kido, M., Inazu, D., Hayashi, Y., Tsushima, H., Hino, R., and Fujimoto, H. Frontal wedge deformation near the source region of the 2011 Tohoku-Oki earthquake. *Geophysical Research Letters*, 38(7), Apr. 2011. doi: 10.1029/2011gl048355.
- Kaiser, A., Balfour, N., Fry, B., Holden, C., Litchfield, N., Gerstenberger, M., D’Anastasio, E., Horspool, N., McVerry, G., Ristau, J., Bannister, S., Christophersen, A., Clark, K., Power, W., Rhoades, D., Massey, C., Hamling, I., Wallace, L., Mountjoy, J., Kaneko, Y., Benites, R., Van Houtte, C., Dellow, S., Wotherpoon, L., Elwood, K., and Gledhill, K. The 2016 Kaikōura, New Zealand, Earthquake: Preliminary Seismological Report. *Seismological Research Letters*, 88(3):727–739, Apr. 2017. doi: 10.1785/0220170018.
- Kluesner, J., Brothers, D., Hart, P., Miller, N., and Hatcher, G. Practical approaches to maximizing the resolution of sparker seismic reflection data. *Marine Geophysical Research*, 40(3):279–301, Sept. 2018. doi: 10.1007/s11001-018-9367-2.
- Kodaira, S., No, T., Nakamura, Y., Fujiwara, T., Kaiho, Y., Miura, S., Takahashi, N., Kaneda, Y., and Taira, A. Coseismic fault rupture at the trench axis during the 2011 Tohoku-oki earthquake. *Nature Geoscience*, 5(9):646–650, Aug. 2012. doi: 10.1038/ngeo1547.
- Kodaira, S., Fujiwara, T., Fujie, G., Nakamura, Y., and Kanamatsu, T. Large Coseismic Slip to the Trench During the 2011 Tohoku-Oki Earthquake. *Annual Review of Earth and Planetary Sciences*, 48(1):321–343, May 2020. doi: 10.1146/annurev-earth-071719-055216.
- Kopp, H. and Kukowski, N. Backstop geometry and accretionary mechanics of the Sunda margin. *Tectonics*, 22(6), Dec. 2003. doi: 10.1029/2002tc001420.
- Li, S., Wang, K., Wang, Y., Jiang, Y., and Dosso, S. E. Geodetically Inferred Locking State of the Cascadia Megathrust Based on a Viscoelastic Earth Model. *Journal of Geophysical Research: Solid Earth*, 123(9):8056–8072, Sept. 2018. doi: 10.1029/2018jb015620.
- Liberty, L. M., Finn, S. P., Haeussler, P. J., Pratt, T. L., and Peterson, A. Megathrust splay faults at the focus of the Prince William Sound asperity, Alaska. *Journal of Geophysical Research: Solid Earth*, 118(10):5428–5441, Oct. 2013. doi: 10.1002/jgrb.50372.
- Lin, Y. N., Sladen, A., Ortega-Culaciati, F., Simons, M., Avouac, J., Fielding, E. J., Brooks, B. A., Bevis, M., Genrich, J., Rietbrock, A., Vigny, C., Smalley, R., and Socquet, A. Coseismic and post-seismic slip associated with the 2010 Maule Earthquake, Chile: Characterizing the Arauco Peninsula barrier effect. *Journal of Geophysical Research: Solid Earth*, 118(6):3142–3159, June 2013. doi: 10.1002/jgrb.50207.
- Lindsey, E. O., Mallick, R., Hubbard, J. A., Bradley, K. E., Almeida, R. V., Moore, J. D. P., Bürgmann, R., and Hill, E. M. Slip rate deficit and earthquake potential on shallow megathrusts. *Nature Geoscience*, 14(5):321–326, May 2021. doi: 10.1038/s41561-021-00736-x.
- Litchfield, N. J., Villamor, P., Dissen, R. J. V., Nicol, A., Barnes, P. M., A. Barrell, D. J., Pettinga, J. R., Langridge, R. M., Little, T. A., Mountjoy, J. J., Ries, W. F., Rowland, J., Fenton, C., Stirling, M. W., Kearse, J., Berryman, K. R., Cochran, U. A., Clark, K. J., Hemphill-Haley, M., Khajavi, N., Jones, K. E., Archibald, G., Upton, P., Asher, C., Benson, A., Cox, S. C., Gasston, C., Hale, D., Hall, B., Hatem, A. E., Heron, D. W., Howarth, J., Kane, T. J., Lamarche, G., Lawson, S., Lukovic, B., McColl, S. T., Madugo, C., Manousakis, J., Noble, D., Pedley, K., Sauer, K., Stahl, T., Strong, D. T., Townsend, D. B., Toy, V., Williams, J., Woelz, S., and Zinke, R. Surface Rupture of Multiple Crustal Faults in the 2016 Mw 7.8 Kaikōura, New Zealand, Earthquake. *Bulletin of the Seismological Society of America*, 108(3B):1496–1520, June 2018. doi: 10.1785/0120170300.
- MacKay, M. E. Structural variation and landward vergence at the toe of the Oregon accretionary prism. *Tectonics*, 14(6): 1309–1320, Dec. 1995. doi: 10.1029/95tc02320.
- Maloney, D., Davies, R., Imber, J., Higgins, S., and King, S. New insights into deformation mechanisms in the gravitationally driven Niger Delta deep-water fold and thrust belt. *AAPG Bulletin*, 94(9):1401–1424, Sept. 2010. doi: 10.1306/01051009080.
- Mannu, U., Ueda, K., Willett, S. D., Gerya, T. V., and Strasser, M. Impact of sedimentation on evolution of accretionary wedges: Insights from high-resolution thermomechanical modeling. *Tectonics*, 35(12):2828–2846, Dec. 2016. doi: 10.1002/2016tc004239.
- Mannu, U., Ueda, K., Willett, S. D., Gerya, T. V., and Strasser, M. Stratigraphic signatures of forearc basin formation mechanisms. *Geochemistry, Geophysics, Geosystems*, 18(6):2388–2410, June 2017. doi: 10.1002/2017gc006810.
- McAdoo, B. G., Orange, D. L., Screamon, E., Lee, H., and Kayen, R. Slope basins, headless canyons, and submarine palaeoseismology of the Cascadia accretionary complex. *Basin Research*, 9(4): 313–324, Dec. 1997. doi: 10.1046/j.1365-2117.1997.00049.x.
- McCalpin, J. P. and Nelson, A. R. *Chapter 1 Introduction to Paleoseismology*, page 1–27. Elsevier, 2009. doi: 10.1016/s0074-6142(09)95001-x.
- McNeill, L. C. and Henstock, T. J. Forearc structure and morphology along the Sumatra–Andaman subduction zone. *Tectonics*, 33(2): 112–134, Feb. 2014. doi: 10.1002/2012tc003264.
- McNeill, L. C., Piper, K. A., Goldfinger, C., Kulm, L. D., and Yeats,

- R. S. Listric normal faulting on the Cascadia continental margin. *Journal of Geophysical Research: Solid Earth*, 102(B6): 12123–12138, June 1997. doi: 10.1029/97jb00728.
- McNeill, L. C., Goldfinger, C., Kulm, L. D., and Yeats, R. S. Tectonics of the Neogene Cascadia forearc basin: Investigations of a deformed late Miocene unconformity. *Geological Society of America Bulletin*, 112(8):1209–1224, Aug. 2000. doi: 10.1130/0016-7606(2000)112<1209:totnfc>2.0.co;2.
- Melgar, D. Was the January 26th, 1700 Cascadia Earthquake Part of a Rupture Sequence? *Journal of Geophysical Research: Solid Earth*, 126(10), Oct. 2021. doi: 10.1029/2021jb021822.
- Mitchum, R. M., Vail, P. R., and Sangree, J. B. *Seismic Stratigraphy and Global Changes of Sea Level, Part 6 Stratigraphic Interpretation of Seismic Reflection Patterns in Depositional Sequences*. American Association of Petroleum Geologists, 1977. doi: 10.1306/m26490c8.
- Moore, J. C. and Saffer, D. Updip limit of the seismogenic zone beneath the accretionary prism of southwest Japan: An effect of diagenetic to low-grade metamorphic processes and increasing effective stress. *Geology*, 29(2):183, 2001. doi: 10.1130/0091-7613(2001)029<0183:ulotsz>2.0.co;2.
- Moore, J. C., Rowe, C., and Meneghini, F. *10. How Accretionary Prisms Elucidate Seismogenesis in Subduction Zones*, page 288–315. Columbia University Press, Dec. 2007. doi: 10.7312/dixo13866-010.
- Morton, E. A., Bilek, S. L., and Rowe, C. A. Cascadia Subduction Zone Fault Heterogeneities From Newly Detected Small Magnitude Earthquakes. *Journal of Geophysical Research: Solid Earth*, 128(6), May 2023. doi: 10.1029/2023jb026607.
- Nedimović, M. R., Bohnenstiehl, D. R., Carbotte, S. M., Pablo Canales, J., and Dziak, R. P. Faulting and hydration of the Juan de Fuca plate system. *Earth and Planetary Science Letters*, 284(1–2):94–102, June 2009. doi: 10.1016/j.epsl.2009.04.013.
- Plafker, G. *Tectonics of the March 27, 1964, Alaska earthquake*. 1969. doi: 10.3133/pp543i.
- Posamentier, H. W., Paumard, V., and Lang, S. C. Principles of seismic stratigraphy and seismic geomorphology I: Extracting geologic insights from seismic data. *Earth-Science Reviews*, 228: 103963, May 2022. doi: 10.1016/j.earscirev.2022.103963.
- Qiu, Q. and Barbot, S. Tsunami excitation in the outer wedge of global subduction zones. *Earth-Science Reviews*, 230:104054, July 2022. doi: 10.1016/j.earscirev.2022.104054.
- Ramos, M. D., Liberty, L. M., Haeussler, P. J., and Humphreys, R. Upper-plate structure and tsunamigenic faults near the Kodiak Islands, Alaska, USA. *Geosphere*, 18(5):1474–1491, July 2022. doi: 10.1130/ges02486.1.
- Riedel, M., Côté, M. M., Urlaub, M., Geersen, J., Scholz, N. A., Naegeli, K., and Spence, G. D. Slope failures along the deformation front of the Cascadia margin: linking slide morphology to subduction zone parameters. *Geological Society, London, Special Publications*, 477(1):47–67, Apr. 2018. doi: 10.1144/sp477.33.
- Ross, W. C., Halliwell, B. A., May, J. A., Watts, D. E., and Syvitski, J. Slope readjustment: A new model for the development of submarine fans and aprons. *Geology*, 22(6):511, 1994. doi: 10.1130/0091-7613(1994)022<0511:sranmf>2.3.co;2.
- Ryan, W. B. F., Carbotte, S. M., Coplan, J. O., O'Hara, S., Melkonian, A., Arko, R., Weissel, R. A., Ferrini, V., Goodwillie, A., Nitsche, F., Bonczkowski, J., and Zemsky, R. Global Multi-Resolution Topography synthesis. *Geochemistry, Geophysics, Geosystems*, 10(3), Mar. 2009. doi: 10.1029/2008gc002332.
- Sakaguchi, A., Chester, F., Curewitz, D., Fabbri, O., Goldsby, D., Kimura, G., Li, C.-F., Masaki, Y., Sreaton, E. J., Tsutsumi, A., Ujiie, K., and Yamaguchi, A. Seismic slip propagation to the up-dip end of plate boundary subduction interface faults: Vitritine reflectance geothermometry on Integrated Ocean Drilling Program NanTro SEIZE cores. *Geology*, 39(4):395–398, Mar. 2011. doi: 10.1130/g31642.1.
- Salmi, M. S., Johnson, H. P., and Harris, R. N. Thermal environment of the Southern Washington region of the Cascadia subduction zone. *Journal of Geophysical Research: Solid Earth*, 122(8):5852–5870, Aug. 2017. doi: 10.1002/2016jb013839.
- Satake, K., Shimazaki, K., Tsuji, Y., and Ueda, K. Time and size of a giant earthquake in Cascadia inferred from Japanese tsunami records of January 1700. *Nature*, 379(6562):246–249, Jan. 1996. doi: 10.1038/379246a0.
- Schmalzle, G. M., McCaffrey, R., and Creager, K. C. Central Cascadia subduction zone creep. *Geochemistry, Geophysics, Geosystems*, 15(4):1515–1532, Apr. 2014. doi: 10.1002/2013gc005172.
- Schmitt, R. G. Quaternary Faults Web Application, 2017. doi: 10.5066/F7S75FJM.
- Seeber, L., Mueller, C., Fujiwara, T., Arai, K., Soh, W., Djajidhardja, Y., and Cormier, M. Accretion, mass wasting, and partitioned strain over the 26 Dec 2004 Mw9.2 rupture offshore Aceh, northern Sumatra. *Earth and Planetary Science Letters*, 263(1–2): 16–31, Nov. 2007. doi: 10.1016/j.epsl.2007.07.057.
- Seely, D. R. *The significance of landward vergence and oblique structural trends on trench inner slopes*, page 187–198. American Geophysical Union, 1977. doi: 10.1029/me001p0187.
- Silver, E. A. Pleistocene tectonic accretion of the continental slope off Washington. *Marine Geology*, 13(4):239–249, Nov. 1972. doi: 10.1016/0025-3227(72)90053-9.
- Simpson, G. D. Formation of accretionary prisms influenced by sediment subduction and supplied by sediments from adjacent continents. *Geology*, 38(2):131–134, Feb. 2010. doi: 10.1130/g30461.1.
- Smith, G., McNeill, L., Henstock, T. J., and Bull, J. The structure and fault activity of the Makran accretionary prism. *Journal of Geophysical Research: Solid Earth*, 117(B7), July 2012. doi: 10.1029/2012jb009312.
- Stevens, D. E., Henstock, T. J., and McNeill, L. C. Evolution of the Thermal and Dehydration State of Sediments Entering the North Sumatra Subduction Zone. *Geochemistry, Geophysics, Geosystems*, 22(4), Apr. 2021. doi: 10.1029/2020gc009306.
- Stone, I., Vidale, J. E., Han, S., and Roland, E. Catalog of Offshore Seismicity in Cascadia: Insights Into the Regional Distribution of Microseismicity and its Relation to Subduction Processes. *Journal of Geophysical Research: Solid Earth*, 123(1):641–652, Jan. 2018. doi: 10.1002/2017jb014966.
- Sun, T., Wang, K., Fujiwara, T., Kodaira, S., and He, J. Large fault slip peaking at trench in the 2011 Tohoku-oki earthquake. *Nature Communications*, 8(1), Jan. 2017. doi: 10.1038/ncomms14044.
- Suppe, J., Chou, G. T., and Hook, S. C. *Rates of folding and faulting determined from growth strata*, page 105–121. Springer Netherlands, 1992. doi: 10.1007/978-94-011-3066-0_9.
- Tobin, H., Kimura, G., and Kodaira, S. Processes Governing Giant Subduction Earthquakes: IODP Drilling to Sample and Instrument Subduction Zone Megathrusts. *Oceanography*, 32(1): 80–93, Mar. 2019. doi: 10.5670/oceanog.2019.125.
- Tobin, H. J. and Kinoshita, M. NanTroSEIZE: The IODP Nankai Trough Seismogenic Zone Experiment. *Scientific Drilling*, 2: 23–27, Mar. 2006. doi: 10.5194/sd-2-23-2006.
- Tobin, H. J., Moore, J. C., Mackay, M. E., Orange, D. L., and Kulm, L. D. Fluid flow along a strike-slip fault at the toe of the Oregon accretionary prism: Implications for the geometry of frontal accretion. *Geological Society of Amer-*

- ica Bulletin*, 105(5):569–582, May 1993. doi: 10.1130/0016-7606(1993)105<0569:ffaass>2.3.co;2.
- Ueda, H., Kitazato, H., Jamieson, A., Bond, T., Cardigos, S., Funaki, M., Maroni, P. J., Nanbu, H., O’Callaghan, J. M., Onishi, T., Pedersen, S. W., Roperez, J., Tsuruzono, H., Watanabe, H. K., and Yasuda, T. The submarine fault scarp of the 2011 Tohoku-oki Earthquake in the Japan Trench. *Communications Earth & Environment*, 4(1), Dec. 2023. doi: 10.1038/s43247-023-01118-4.
- Ulrich, T., Gabriel, A.-A., Ampuero, J.-P., and Xu, W. Dynamic viability of the 2016 Mw 7.8 Kaikōura earthquake cascade on weak crustal faults. *Nature Communications*, 10(1), Mar. 2019. doi: 10.1038/s41467-019-09125-w.
- Underwood, M. B. Strike-parallel variations in clay minerals and fault vergence in the Cascadia subduction zone. *Geology*, 30(2):155, 2002. doi: 10.1130/0091-7613(2002)030<0155:spvicm>2.0.co;2.
- van Zelst, I., Rannabauer, L., Gabriel, A., and van Dinther, Y. Earthquake Rupture on Multiple Splay Faults and Its Effect on Tsunamis. *Journal of Geophysical Research: Solid Earth*, 127(8), Aug. 2022. doi: 10.1029/2022jb024300.
- von Huene, R., Miller, J. J., and Krabbenhoef, A. The Alaska Convergent Margin Backstop Splay Fault Zone, a Potential Large Tsunami Generator Between the Frontal Prism and Continental Framework. *Geochemistry, Geophysics, Geosystems*, 22(1), Jan. 2021. doi: 10.1029/2019gc008901.
- Wang, K. and Hu, Y. Accretionary prisms in subduction earthquake cycles: The theory of dynamic Coulomb wedge. *Journal of Geophysical Research: Solid Earth*, 111(B6), June 2006. doi: 10.1029/2005jb004094.
- Watt, J. T. and Brothers, D. S. Systematic characterization of morphotectonic variability along the Cascadia convergent margin: Implications for shallow megathrust behavior and tsunami hazards. *Geosphere*, 17(1):95–117, Nov. 2020. doi: 10.1130/ges02178.1.
- Wendt, J., Oglesby, D. D., and Geist, E. L. Tsunamis and splay fault dynamics. *Geophysical Research Letters*, 36(15), Aug. 2009. doi: 10.1029/2009gl038295.
- Wilson, A. and Ma, S. Wedge Plasticity and Fully Coupled Simulations of Dynamic Rupture and Tsunami in the Cascadia Subduction Zone. *Journal of Geophysical Research: Solid Earth*, 126(7), July 2021. doi: 10.1029/2020jb021627.
- Witter, R. C., Zhang, Y. J., Wang, K., Priest, G. R., Goldfinger, C., Stimely, L., English, J. T., and Ferro, P. A. Simulated tsunami inundation for a range of Cascadia megathrust earthquake scenarios at Bandon, Oregon, USA. *Geosphere*, 9(6):1783–1803, Dec. 2013. doi: 10.1130/ges00899.1.
- Xu, S., Fukuyama, E., Ben-Zion, Y., and Ampuero, J.-P. Dynamic rupture activation of backthrust fault branching. *Tectonophysics*, 644–645:161–183, Mar. 2015. doi: 10.1016/j.tecto.2015.01.011.
- Yamaguchi, A., Sakaguchi, A., Sakamoto, T., Iijima, K., Kameda, J., Kimura, G., Ujiie, K., Chester, F. M., Fabbri, O., Goldsby, D., Tsutsumi, A., Li, C.-F., and Curewitz, D. Progressive illitization in fault gouge caused by seismic slip propagation along a megasplay fault in the Nankai Trough. *Geology*, 39(11):995–998, Oct. 2011. doi: 10.1130/g32038.1.

The article *Late Quaternary Surface Displacements on Accretionary Wedge Splay Faults in the Cascadia Subduction Zone: Implications for Megathrust Rupture* © 2024 by A.M. Ledeczi is licensed under CC BY 4.0.